Journal of Geochemical Exploration 167 (2016) 83–109

Contents lists available at ScienceDirect

Journal of Geochemical Exploration

journal homepage: www.elsevier.com/locate/gexplo

Phyllosilicates geochemistry and distribution in the Altar porphyry Cu-(Au) deposit, Andes Cordillera of San Juan, Argentina: Applications in exploration, geothermometry, and geometallurgy

Laura Maydagán [a,b,*], Marta Franchini [a,c,d], Agnes Impiccini [d], David Lentz [e]

[a] Centro Patagónico de Estudios Metalogenéticos-CONICET, Argentina
[b] INGEOSUR-CONICET, Departamento de Geología, Universidad Nacional del Sur, San Juan 670, 8000 Bahía Blanca, Argentina
[c] Instituto de Investigación en Paleobiología y Geología, Universidad Nacional de Río Negro, Av. Roca 1242, 8332, Roca, Argentina
[d] Departamento de Geología y Petróleo, Facultad de Ingeniería, Universidad Nacional del Comahue, Buenos Aires 1400, 8300 Neuquén, Argentina
[e] Department of Earth Sciences, University of New Brunswick, Fredericton, New Brunswick, E3B 5A3, Canada

ARTICLE INFO

Article history:
Received 3 December 2015
Revised 15 April 2016
Accepted 1 May 2016
Available online 6 May 2016

Keywords:
Phyllosilicates
Clays
Altar porphyry
Argentina
Mining exploration
Geometallurgy

ABSTRACT

Biotite, chlorite, muscovite, illite, and kaolinite from the Altar porphyry Cu-(Au) deposit of the Andean Main Cordillera of San Juan Province (Argentina) were constrained using X-ray diffraction, electron microprobe, and infrared spectroscopy analyses to map compositional variations.

Magmatic and hydrothermal biotites from the andesite-dacite mineralized porphyries have higher X_{Mg}, K, and F contents and lower Fe/(Fe + Mg) ratios compared to the magmatic biotites from the andesite-dacite barren porphyries of the district Hydrothermal biotites from deep levels with potassic alteration and high Cu grades have the highest X_{Mg} ratios and high F contents. The similarity of the log fH_2O/fHF, log $fHF/fHCl$, and log $fH_2O/fHCl$ fugacity ratios of biotites from Altar mineralized porphyries and from the neighbouring Los Pelambres porphyry copper deposit suggests that these parameters may be a function of the magmatic source. Chlorite crystals associated with Cu mineralization (0.2 to 1.2% Cu) show lower Fe and Mn and higher Mg contents than chlorite from shallow and distal zones. Potassic dioctahedral phyllosilicates are the most abundant phyllosilicates in the Altar deposit, occur in the phyllic and chloritic zones, and are superimposed on potassic alteration. In zones of high copper grades (>0.8% Cu), potassic dioctahedral phyllosilicates have total Al (apfu) between 2.4 and 2.8 and intermediate compositions between muscovite, phengitic muscovite, and illite, whereas those with higher and lower Al contents come from zones with lower Cu grades.

Temperatures obtained from X_{Mg}-Ti equilibria in biotite (691–800 °C) and ^{IV}Al occupancy in chlorite (214–340 °C), agree with previous temperature estimates based on Ti in quartz and fluid inclusion microthermometry. Muscovite is stable at temperatures higher than ~300 °C, whereas phengitic muscovite indicates temperatures between 280 and 400 °C and higher K^+/H^+ conditions (less acidic environment) compared to muscovite. Illite represents a younger and cooler (220 to 310 °C) hydrothermal alteration event, and kaolinite in late veins halos reflects a decrease of the temperature (<200 °C) of late hydrothermal fluids.

Our study demonstrates that variations in phyllosilicate composition have the potential to be used as vectors in ore exploration and to differentiate between barren and fertile intrusions. A detailed analysis of type and proportion of phyllosilicates, as well as the presence of ore minerals in fine fractions, should be undertaken to optimize metal recoveries during the upcoming benefaction of these ores.

1. Introduction

Early studies of porphyry copper systems have used the geochemical and mineralogical zoning patterns of these deposits as a footprint guide for exploration (e.g., Meyer and Hemley, 1967; Lowell and Guilbert, 1970; Gustafson and Hunt, 1975; Dilles and Einaudi, 1992). However, understanding the controls on the formation of these alteration zones, discriminating mineralized and barren environments and recognizing the centers and fringes of the ore systems continue to be great challenges to the exploration industry (Wilkinson et al., 2015).

Recent investigations in porphyry copper deposits showed that white mica compositions and illite crystallinity can be used to map fluid temperature and pH gradients and to predict unexposed mineralization zones in areas where the surface has a strong supergene overprint (e.g., Franchini et al., 2007; Cohen, 2011). Trace elements are enriched in phyllosilicates along a near-vertical pathway of the magmatic hydrothermal plume extending from the ore zone of the

* Corresponding author.
E-mail address: lauramaydagan@yahoo.com.ar (L. Maydagán).

http://dx.doi.org/10.1016/j.gexplo.2016.05.002
0375-6742/

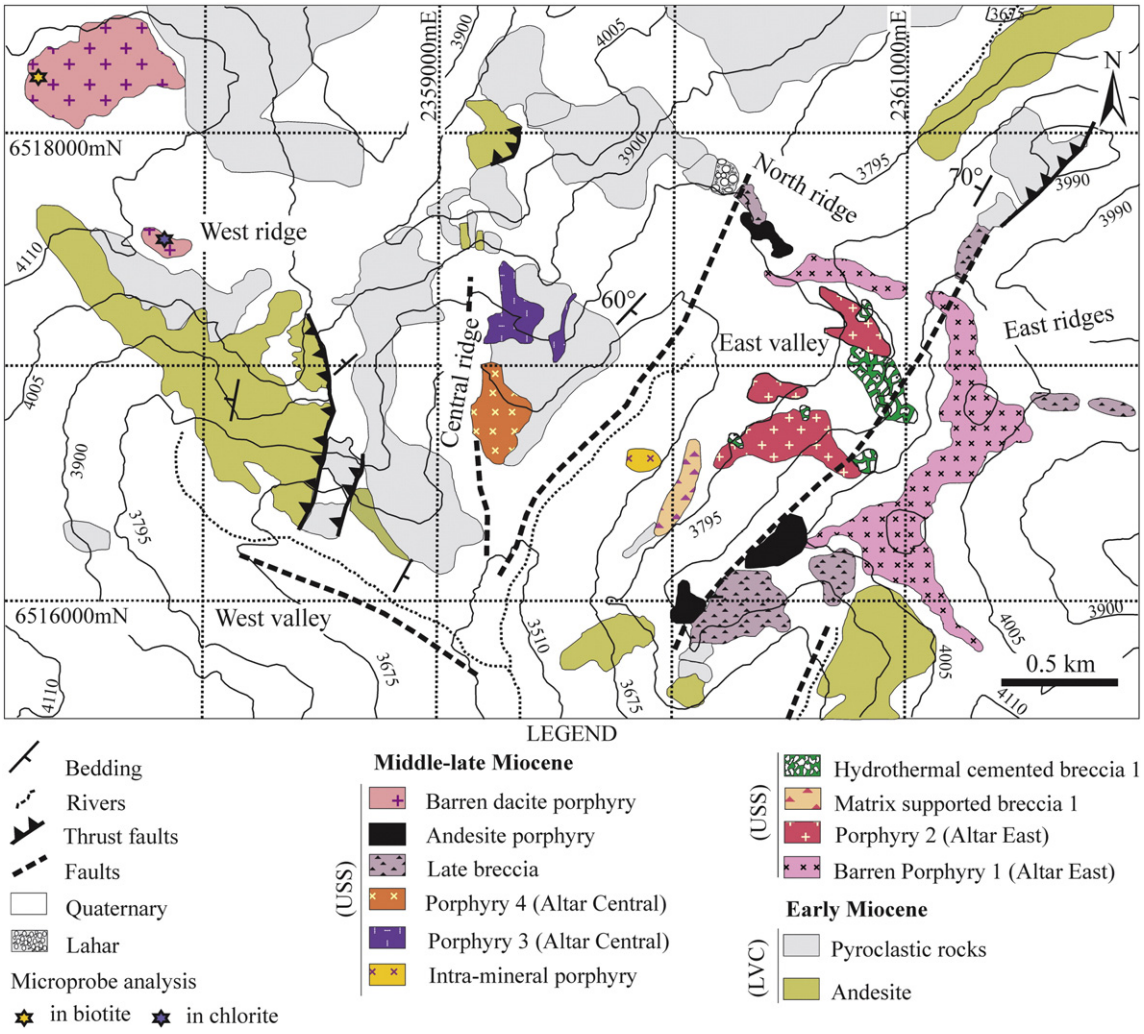

Fig. 1. Detailed map of Altar geology. Locations are given in Gauss Krueguer coordinates, Inchauspe. Locations of biotite and chlorite samples from outcrops are shown. LVC: lower volcanic complex, USS: upper subvolcanic suite (modified from Maydagán et al., 2011).

porphyry deposit upward to the surface environment (e.g., W, Sn and Tl in muscovite and Li in chlorite, Cohen, 2011). A variety of elements, including K, Li, Mg, Ca, Sr, Ba, Ti, V, Mn, Co, Ni, Zn and Pb are probably incorporated in the chlorite lattice and display systematic spatial variations relative to the porphyry center (Wilkinson et al., 2015). In addition, the mineralogy and distribution of phyllosilicates have implications in the metallurgy of these ores (Bulatovic et al., 1999). However, few studies document in detail the compositional variations and distribution of these minerals within ore deposits.

The Altar porphyry Cu-(Au) deposit (31° 29′ S, 70° 28′ W), located in the Cordillera Principal of SW San Juan Province, Argentina, is a large copper deposit (995 Mt, 0.35% Cu, 0.083 g/t Au; Marek, 2014) and is one of the few examples in the world in which it is possible to observe the transition between the epithermal high sulfidation siliceous ledges and the associated porphyry deposit. Maydagán et al. (2011, 2014) conducted the first geological mapping, geochronologic and geochemical investigation of the Altar magmatic rocks. A subsequent study of the different generations of Altar veins based on cathodoluminescence (CL) imaging, trace elements in quartz, and fluid inclusion microthermometry permitted differentiate quartz generations precipitated during different mineralization and alteration events and relate sulfides to a specific generation of quartz (Maydagán et al., 2015). In this contribution we present a detailed mineralogical study of phyllosilicates, clays, and their distribution along the best explored sections of the Altar deposit. The objective is to provide information on these hydrothermal minerals necessary to precisely document the thermal and chemical evolution of the Altar hydrothermal system, try to identify vectors for ore exploration and to optimize benefaction of metals from orebody metallurgy management.

2. Regional geology

The Altar region is located in the Andean Main Cordillera over the flat-slab segment (27–33° S) of the Southern Central Andes. The subducting slab in this segment has a relatively smooth transition to the north, toward the Central Volcanic Zone, and a southerly transition to segments with a steeper subduction angle (30°; Cahill and Isacks, 1992; Anderson et al., 2007; Gans et al., 2011). From 35 to 21 Ma, in the western part of the Cordillera Principal between 32° and 37° S, thick volcano-sedimentary sequences accumulated under an extensional tectonic regime (Charrier et al., 2002) in volcano-tectonic depressions or intra-arc basins, which in the study region is the Abanico basin (Muñoz et al., 2006; Mpodozis and Cornejo, 2012). These sequences were assigned to Abanico, Coya-Machalí, and Cura-Mallín formations (e.g., Jordan et al., 2001; Charrier et al., 2002; Kay et al., 2005; Farías et al., 2008). During the early Miocene (27–20 Ma), this segment had a subducted slab geometry similar to that currently observed in the normal-slab segment at 35° S, and a crustal thickness of 35–40 km

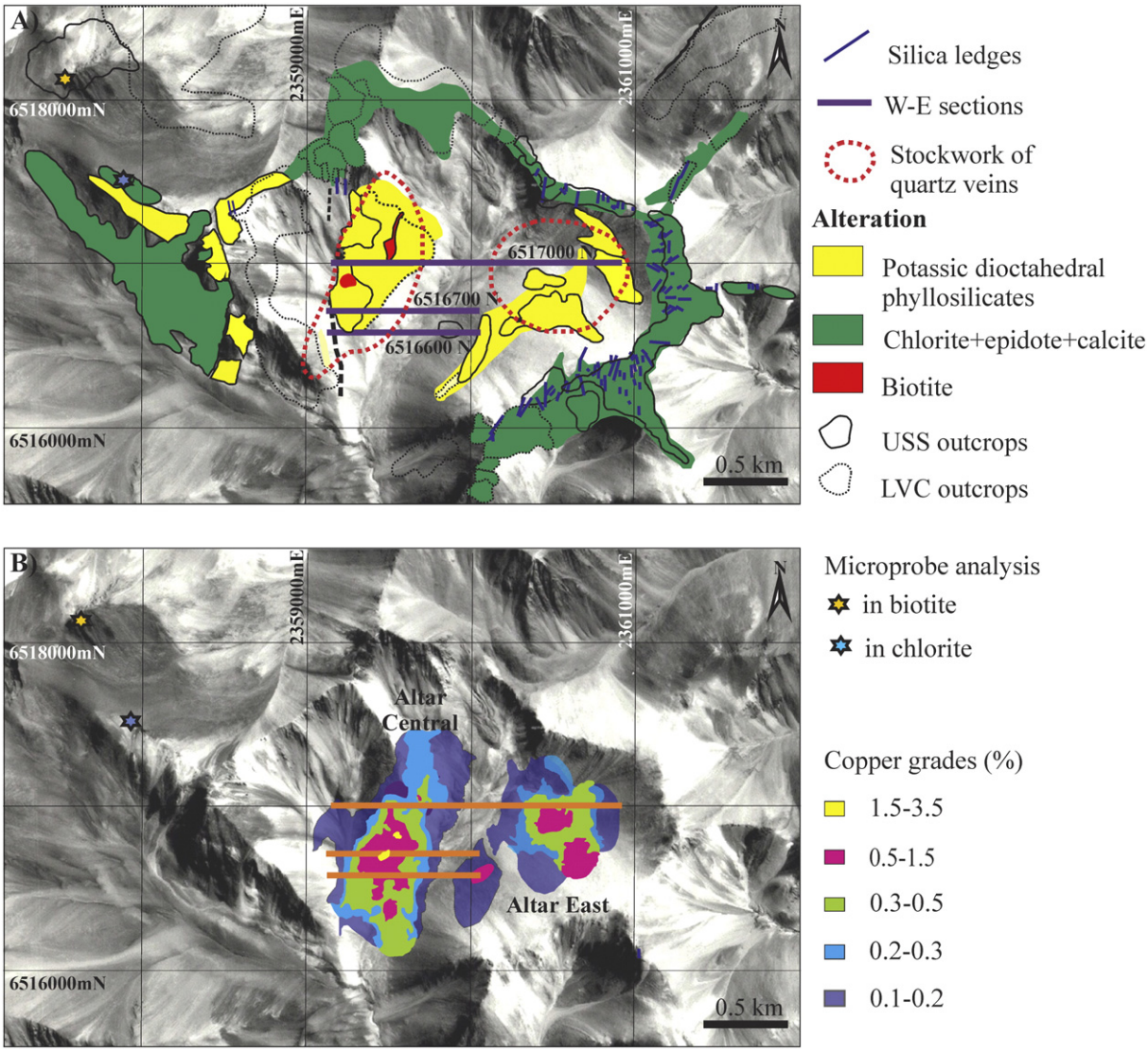

Fig. 2. A) Map with the distribution of phyllosilicates based on detailed geological mapping and location of the three sections analyzed (modified from Maydagán et al., 2015). B) Cu distribution map obtained considering the copper grades of the drill holes below the leaching zone (Marek, 2014; Maydagán et al., 2015). USS: upper subvolcanic suite, LVC: lower volcanic complex. Locations of biotite and chlorite samples from outcrops are shown.

(Kay and Mpodozis, 2002). The shallowing of the subduction zone progressed from middle to late Miocene (20–5 Ma), accompanied by the subduction of the Juan Fernández ridge (e.g., Yáñez et al., 2001) and eastward migration and broadening of the arc (Kay and Mpodozis, 2002). The emplacement of the porphyries took place under a compressive regime and crustal shortening. Basin inversion and significant tectonic uplift of the Principal Andean Cordillera occurred as a result of the Neogene compressive tectonism (Maksaev et al., 2009). Cessation of the magmatic activity over the flat-slab Miocene arc occurred at 5 Ma. Subsequent magmatism over the flat-slab was present in the back-arc, in particular the Farallón Negro, Pocho, and San Luis magmatic centers (Kay and Mpodozis, 2002).

3. Local Geology

Maydagán et al. (2011) presented the first complete geological mapping, geochemical, and geochronologic studies of the igneous rocks of the Altar region. The Altar lower volcanic complex (Fig. 1) is composed of basaltic andesite and andesite-dacite lava flows, lapilli tuff, and pyroclastic breccia, and grades upwards to an upper unit of compacted and thick massive tuff. The lower volcanic complex is part of an early Miocene magmatic arc (20.8 Ma ± 0.3 Ma and 21.6 ± 1.2 Ma; U-Pb ages, Maydagán et al., 2011; Maydagán, 2012) formed above a normal subduction zone whose magmas underwent fractional crystallization and crustal contamination.

The Altar subvolcanic suite consists of a series of barren and copper-bearing intrusions and breccias (Fig. 1) that intrude the lower volcanic complex and represent a middle-late Miocene magmatic arc formed above a shallow subduction zone (Maydagán et al., 2011). LA-ICPMS U-Pb ages in zircons from the Altar porphyries indicate four discrete events of intrusions over an extended magmatic life time of ca. 3 m·y (Maydagán et al., 2014). The suite comprises a pre-mineralization porphyry (barren porphyry 1), three mineralized porphyries (porphyries 2, 3 and 4), two barren intrusions (andesite porphyry and barren dacite porphyry), and a postmineralization breccia (Late breccia, Fig. 1). The modal composition of both barren and fertile less altered samples is similar and ranges from dacite (with quartz phenocrysts) to andesite, and consist of plagioclase + amphibole ± biotite ± quartz

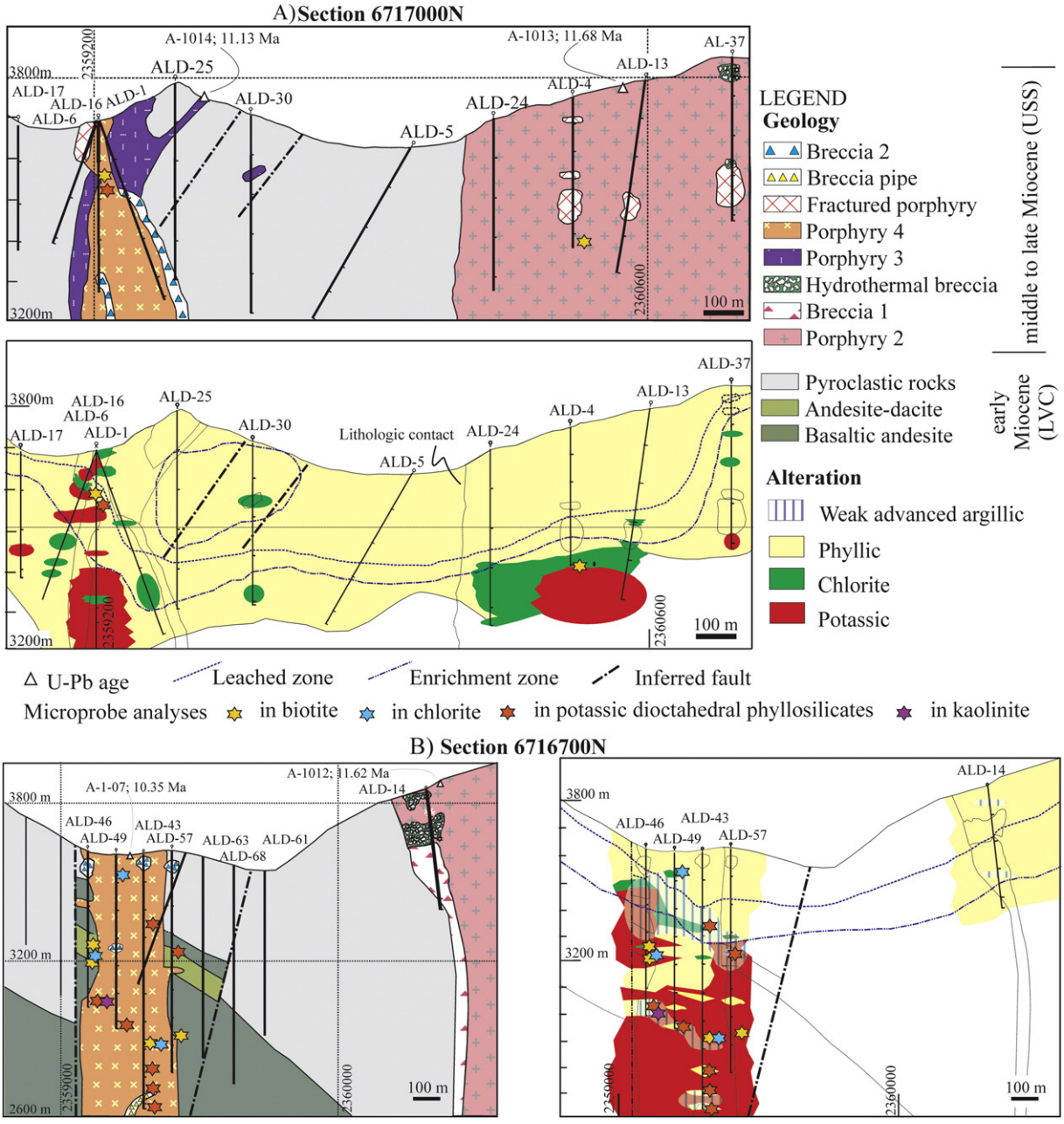

Fig 3. Geological W-E sections 6717000 mN and 6716700 mN and hydrothermal alterations distribution (modified from Maydagán et al., 2015). Location of samples analyzed by electron microprobe is shown.

phenocrysts with apatite + ulvöspinel ± magnetite as accessory minerals in an aphanitic groundmass (Maydagán et al., 2011).

3.1. Petrography of barren intrusions

Barren porphyry 1 (11.75 ± 0.24 Ma, Maydagán et al., 2011) crops out on the eastern ridges of the Altar district at elevations of 4000 m, where is cut by Au-(Ag-Cu) epithermal veins (Fig. 1). It is the largest porphyry with a surface area of ~1 km^2. Phenocrysts of plagioclase (30 − 60 vol%, 0.1 − 7 mm), edenite (2 − 15 vol%), accessory spinel minerals ("magnetite-ulvöspinel solid solution," 1 − 1.5 vol%), apatite, and zircon are set in a fine-grained (<40 μm) quartz + feldspar + magnetite groundmass. Barren porphyry 1 has been affected by weak to moderate propylitic alteration.

A barren dacite porphyry is exposed in the northwest section of the Altar area (Fig. 1). The porphyritic texture is defined by phenocrysts of oligoclase, amphibole, biotite, with accessory ulvöspinel, apatite, and zircon, set in a microcrystalline (0.01 − 0.05 mm) quartz + feldspar ± ulvöspinel groundmass. This porphyry has been affected by propylitic alteration or is fresh and has no veins.

3.2. Petrography of fertile intrusions

Porphyry 2 crops out on the east valley (11.62 ± 0.21 and 11.68 ± 0.27 Ma, Maydagán et al., 2014, Fig. 1) where it occurs as a stock (~0.5 km^2) that cuts tuffs of the lower volcanic complex. Porphyry 2 contains phenocryst of plagioclase (45 − 50 vol%), edenite (3 − 10 vol%), biotite (1 vol%), and accessory quartz, magnetite, and zircon set in a coarse-grained (100 − 200 μm) hydrothermal quartz + feldspar + biotite groundmass. Porphyry 3 (11.13 ± 0.26 Ma, Maydagán et al., 2014) crops out on the central ridge (Fig. 1) where occurs as a stock (~0.3 km^2) and related dikes that cut tuffs of the lower volcanic complex.

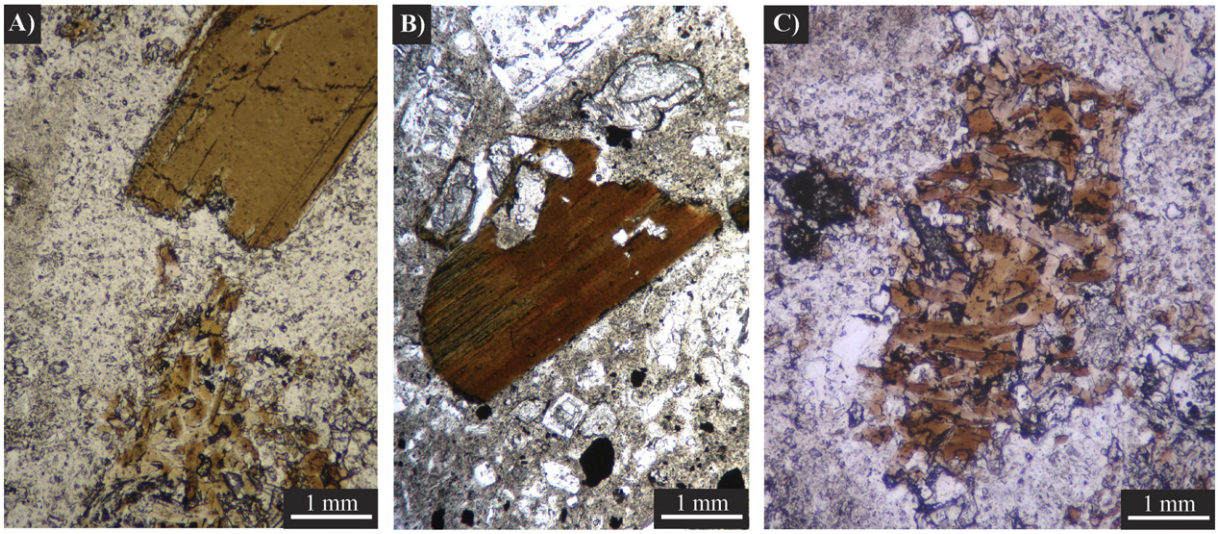

Fig. 4. Photomicrographs in Plane Polarized Light of; A) magmatic and hydrothermal biotite from the potassic alteration of porphyry 4; B) Magmatic biotite from the barren dacite porphyry; C) Hydrothermal biotite from porphyry 4 that have replaced a magmatic amphibole.

Porphyry 3 contains phenocrysts of plagioclase (45 − 50 vol%), edenite (3 − 10 vol%), biotite (1 vol%), and accessory quartz, magnetite, and zircon set in a coarse-grained (100 − 200 μm) hydrothermal quartz + feldspar + biotite groundmass. Porphyry 3 contains 2 to 10 vol% quartz veins and has undergone moderate potassic, sodic, and locally intense phyllic alteration and moderate Cu-Au mineralization. Porphyry 4 (10.35 ± 0.32 Ma, Maydagán et al., 2011) crops out on the southern portion of the central ridge (Fig. 1), where it has intruded the volcanic wall rocks. It contains phenocrysts of plagioclase (60 − 70 vol%, 0.1–5 mm), biotite (1 vol%, <1 cm), and accessory zircon in a groundmass altered to an aggregate (100 − 400 μm) of hydrothermal quartz. Porphyries 2, 3 and 4 have been affected by pervasive potassic alteration at depth and phyllic alteration at shallow levels and contain copper mineralization. Porphyry 4 has the highest copper grades of the Altar district.

3.3. Altar hydrothermal system

Early potassic alteration is associated with quartz + biotite + rutile ± magnetite veinlets (EB veinlets), quartz ± chalcopyrite ± pyrite

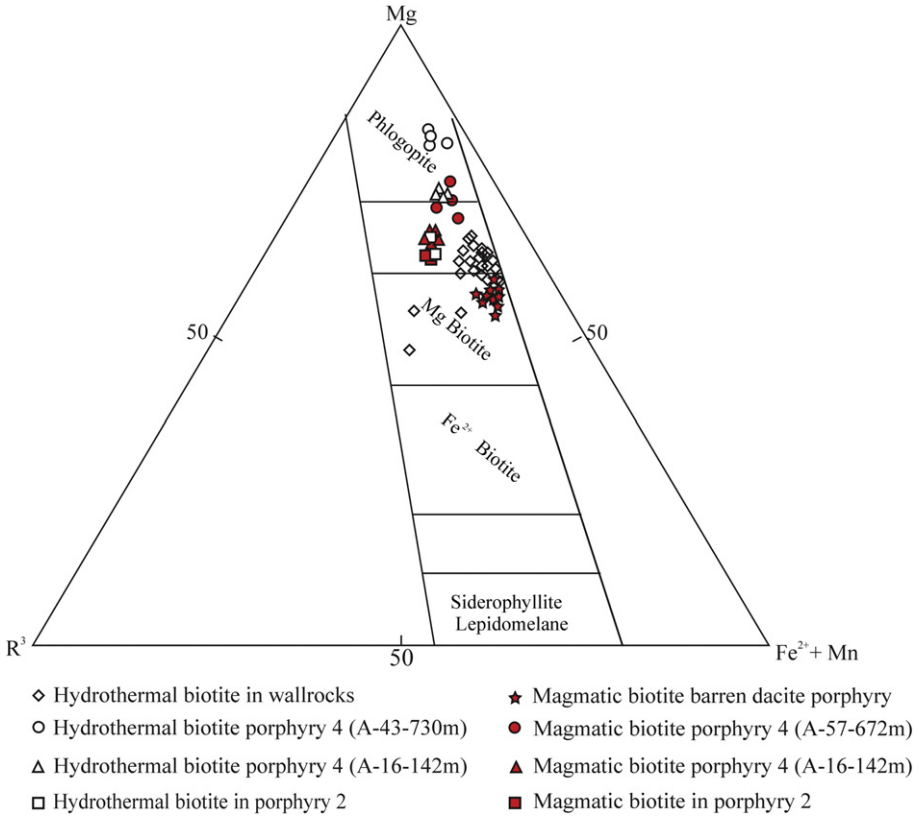

Fig. 5. Diagram of Foster (1962) illustrating the compositions of magmatic and hydrothermal biotites analysed.

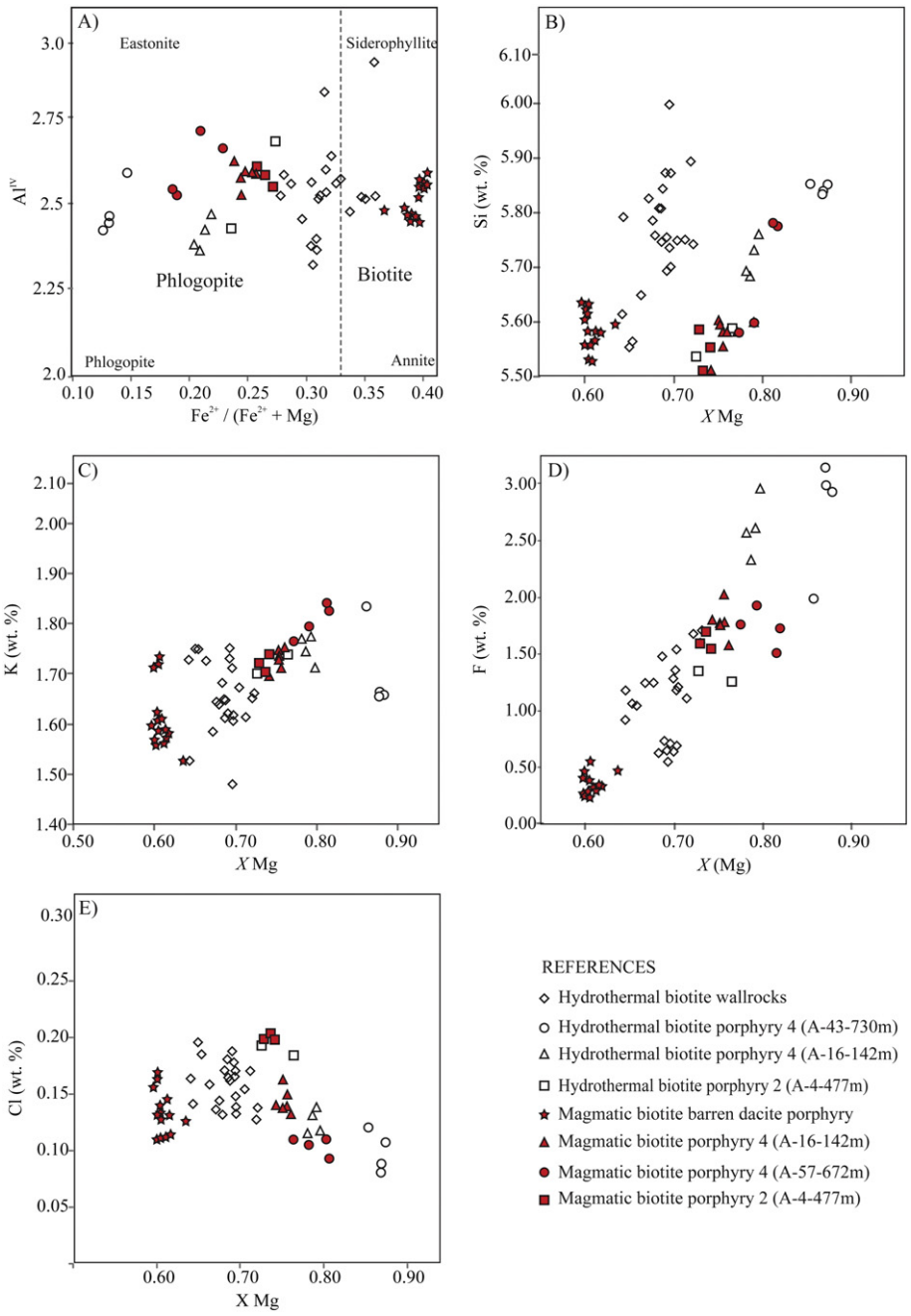

Fig. 6. Compositions of magmatic and hydrothermal biotite A) Al^{IV} versus Fe/(Fe + Mg), B–E) Si, K, F, Cl (wt.%) versus X_{Mg} for Altar biotite.

veins (A veins), and quartz ± molybdenite veins (B veins). Chloritic alteration is associated to chlorite + rutile ± hematite (C veins) veins. Phyllic alteration forms a continuous halo associated to quartz + pyrite veins (D veins) that are surrounded by propylitic alteration on the high ridges around the project. Late veins and veinlets rich in sulfides and sulfosalts (E veins: tennantite quartz ± pyrite ± gold ± pyrite ± quartz; enargite + pyrite ± quartz) with irregular halos of kaolinite ± quartz ± rutile overlapped the deep and intermediate high-temperature veins. In the eastern zone of the Altar deposit, high sulfidation epithermal siliceous ledges (chalcedony ± gold, and quartz ± alunite ± enargite ± gold, native sulfur and barite) occur on the high ridges above the porphyry deposit, whereas in the central orebody, epithermal veins (E veins or equivalent to epithermal) overlap the porphyry veinlets. The uplift of the land in the central Altar orebody would have increased the overlapping of late low-temperature and early high-temperature veins (Maydagán et al., 2015).

4. Analytical techniques and sampling methodology

Field data were collected from examination of outcrops and approximately 10,000 m of core from 25 selected drill holes chosen from three cross sections across the currently best explored ore zone (Fig. 2).

Polished thin sections of 210 samples corresponding to the different lithologies, alteration zones, mineralization, and veins were studied by transmitted and reflected light petrography. In the mineral assemblages, the minerals are listed and separated by the symbol (+), if they are in equal amounts and with (±) if the mineral is in minor

Table 1
Representative microprobe analyses of magmatic biotite and hydrothermal biotite.

Sample no.	ALD-156	ALD-156	ALD-156	ALD-156	ALD-156	ALD-156	ALD-156	ALD-156	ALD-156	ALD-156	ALD-156	ALD-156	ALD-156	ALD-156	ALD-156	ALD-46	ALD-46	ALD-46
Depth (m)	Surface	Surface	Surface	Surface	Surface	Surface	Surface	Surface	Surface	Surface	Surface	Surface	Surface	Surface	Surface	321	321	321
	1	2	3	4	5	6	7	8	9	10	11	12	13	14	15	1	2	3
Lithology	Barren dac	Barren dac	Barren dac	Barren dac	Barren dac	Barren dac	Barren dac	Barren dac	Barren dac	Barren dac	Barren dac	Barren dac	Barren dac	Barren dac	Barren dac	Pyroclas.	Pyroclas.	Pyroclas.
Alteration	Fresh	Fresh	Fresh	Fresh	Fresh	Fresh	Fresh	Fresh	Fresh	Fresh	Fresh	Fresh	Fresh	Fresh	Fresh	Potas,Chl.	Potas,Chl.	Potas,Chl.
Origin	Mag.	Mag.	Mag.	Mag.	Mag.	Mag.	Mag.	Mag.	Mag.	Mag.	Mag.	Mag.	Mag.	Mag.	Mag.	Hyd.	Hyd.	Hyd.
SiO_2	36.34	36.26	36.48	36.87	36.74	36.13	36.95	35.84	35.53	36.37	35.86	36.53	37.52	37.01	37.13	42.32	39.55	39.70
TiO_2	3.67	3.85	3.77	3.75	3.70	4.10	3.87	3.52	3.46	3.54	3.51	3.52	3.68	3.74	3.71	2.31	3.45	3.15
Al_2O_3	13.32	13.47	13.41	13.64	13.69	13.47	13.71	13.66	13.42	13.96	13.68	13.82	14.42	14.36	14.07	18.04	14.53	14.76
[1]FeO	16.62	16.26	16.33	16.39	16.19	16.52	15.33	16.05	15.59	15.95	15.80	16.22	17.13	16.89	16.89	10.61	11.80	12.30
MnO	0.16	0.17	0.20	0.22	0.18	0.20	0.18	0.18	0.15	0.19	0.17	0.18	0.04	0.02	0.05	0.17	0.14	0.17
MgO	14.22	14.31	14.43	14.63	14.59	14.35	14.90	13.49	13.32	13.22	13.42	13.72	14.39	14.43	14.50	13.50	17.15	17.08
CaO	0.01	0.01	0.01	0.01	0.00	0.00	0.09	0.07	0.03	0.05	0.03	0.02	0.02	0.01	0.02	0.20	0.04	0.02
Na_2O	1.08	1.05	0.95	0.90	0.96	0.87	1.01	0.83	0.72	0.81	0.79	0.89	0.81	0.78	0.73	0.65	0.22	0.17
K_2O	8.11	7.99	8.16	8.16	8.18	8.26	7.92	7.86	7.97	8.09	8.14	7.94	9.07	9.03	9.09	8.21	8.99	8.74
F	0.39	0.32	0.33	0.34	0.35	0.34	0.47	0.28	0.27	0.42	0.28	0.28	0.47	0.29	0.56	1.54	1.71	1.68
Cl	0.11	0.11	0.15	0.13	0.11	0.13	0.13	0.16	0.14	0.16	0.13	0.17	0.11	0.13	0.13	0.14	0.14	0.17
Total	94.68	94.38	94.81	95.69	95.32	94.98	95.22	92.60	91.22	93.28	92.38	93.93	97.44	96.55	96.60	97.28	97.24	97.58
Structural formulae based on 22 oxygen atoms																		
Tetrahedral																		
^{IV}Si	5.58	5.57	5.58	5.58	5.58	5.53	5.60	5.60	5.63	5.64	5.61	5.62	5.56	5.53	5.56	6.00	5.74	5.75
^{IV}Al	2.41	2.44	2.42	2.43	2.45	2.43	2.45	2.52	2.51	2.55	2.52	2.51	2.52	2.53	2.48	3.01	2.49	2.52
Octahedral																		
^{VI}Al	0.00	0.00	0.00	0.00	0.00	0.00	0.00	0.05	0.08	0.10	0.08	0.18	0.06	0.00	0.00	0.80	0.06	0.06
Ti	0.42	0.44	0.43	0.43	0.42	0.47	0.44	0.41	0.41	0.41	0.41	0.41	0.41	0.42	0.42	0.25	0.38	0.34
Fe	2.14	2.09	2.09	2.08	2.06	2.11	1.94	2.10	2.07	2.07	2.07	2.09	2.12	2.11	2.11	1.26	1.43	1.49
Mn	0.02	0.02	0.03	0.03	0.02	0.03	0.02	0.02	0.02	0.02	0.02	0.02	0.00	0.00	0.01	0.02	0.02	0.02
Mg	3.26	3.27	3.29	3.30	3.30	3.27	3.36	3.14	3.15	3.05	3.13	3.15	3.18	3.22	3.23	2.85	3.71	3.69
ΣVI	*5.83*	*5.83*	*5.84*	*5.85*	*5.84*	*5.85*	*5.81*	*5.80*	*5.78*	*5.75*	*5.77*	*5.80*	*5.79*	*5.81*	*5.81*	*5.39*	*5.77*	*5.81*
K	1.59	1.56	1.59	1.58	1.59	1.61	1.53	1.57	1.61	1.60	1.63	1.56	1.72	1.72	1.74	1.48	1.67	1.62
Ca	0.00	0.00	0.00	0.00	0.00	0.00	0.01	0.01	0.01	0.01	0.00	0.00	0.00	0.00	0.00	0.03	0.01	0.00
Na	0.32	0.31	0.28	0.26	0.28	0.26	0.30	0.25	0.22	0.24	0.24	0.27	0.23	0.23	0.21	0.18	0.06	0.05
Σ Interlayer	*1.91*	*1.88*	*1.88*	*1.84*	*1.87*	*1.87*	*1.86*	*1.84*	*1.84*	*1.86*	*1.87*	*1.83*	*1.95*	*1.95*	*1.95*	*1.72*	*1.74*	*1.67*
F	0.19	0.15	0.16	0.16	0.17	0.17	0.22	0.14	0.13	0.20	0.14	0.14	0.22	0.14	0.26	0.68	0.77	0.75
Cl	0.03	0.03	0.04	0.03	0.03	0.03	0.03	0.04	0.04	0.04	0.03	0.04	0.03	0.03	0.03	0.03	0.03	0.04
X(Mg)	0.60	0.61	0.61	0.61	0.62	0.61	0.63	0.60	0.60	0.60	0.60	0.60	0.60	0.60	0.60	0.69	0.72	0.71
T (°C)	740	748	745	743	743	754	752	736	736	734	736	734	734	739	738	691	759	744
Fe/(Fe + Mg)	0.40	0.39	0.39	0.39	0.38	0.39	0.37	0.40	0.40	0.40	0.40	0.40	0.40	0.40	0.40	0.31	0.28	0.29

1. All iron as Fe^{2+}, 2.T(°C) Based on geothermometer of Henry et al. (2005), ΣVI: sum of octahedral cations. Abbreviations: Barren dac: barren dacite porphyry; Chl: chloritic; Hyd: hydrothermal; Mag: magmatic; Porph: porphyry; Potas: potassic; Pyroclas: Pyroclastic rock.

Table 1 (*continued*)

Sample no.	ALD-46	ALD-46	ALD-46	ALD-46	ALD-46	ALD-46	ALD-46	ALD-46	ALD-46	ALD-46	ALD-46	ALD-46	ALD-46	ALD-43	ALD-43	ALD-43	ALD-43	ALD-43	ALD-43	ALD-43
Depth (m)	321	321	321	321	321	321	321	397	397	397	397	397	397	690	690	690	690	690	690	690
	4	5	6	7	8	9	10	1	2	3	4	5	6	1	2	3	4	5	6	7
Lithology	Pyroclas.	Pyroclas.	Pyroclas.	Pyroclas.	Pyroclas.	Pyroclas.	Pyroclas.	Andesite	Andesite	Andesite	Andesite	Andesite	Andesite	Andesite	Andesite	Andesite	Andesite	Andesite	Andesite	Andesite
Alteration	Potas,Chl.	Potas,Chl.	Potas,Chl.	Potas,Chl.	Potas,Chl.	Potas,Chl.	Potas,Chl.	Potas,Chl.	Potas,Chl.	Potas,Chl.	Potas,Chl.	Potas,Chl.	Potas,Chl.	Potas,Chl.	Potas,Chl.	Potas,Chl.	Potas,Chl.	Potas,Chl.	Potas,Chl.	Potas,Chl.
Origin	Hyd.	Hyd.	Hyd.	Hyd.	Hyd.	Hyd.	Hyd.	Hyd.	Hyd.	Hyd.	Hyd.	Hyd.	Hyd.	Hyd.	Hyd.	Hyd.	Hyd.	Hyd.	Hyd.	Hyd.
SiO_2	40.60	36.39	38.00	35.87	38.46	38.12	38.99	38.05	38.45	37.83	36.89	36.32	36.91	40.37	39.30	38.70	37.52	39.56	39.49	37.82
TiO_2	2.83	2.25	2.51	3.10	3.07	3.05	3.07	3.08	3.42	3.44	4.00	3.78	3.59	3.37	2.85	3.22	2.52	3.02	2.53	2.77
Al_2O_3	14.87	13.91	14.01	13.15	16.05	13.32	13.93	13.30	13.08	13.18	13.95	13.74	13.86	14.57	14.69	14.31	15.33	14.17	14.38	13.76
^{1}FeO	11.36	12.62	13.17	13.82	13.16	13.00	12.74	13.44	13.25	13.25	14.88	14.52	14.95	12.95	12.94	13.15	12.05	12.55	12.40	12.69
MnO	0.11	0.05	0.09	0.08	0.06	0.07	0.06	0.06	0.09	0.09	0.09	0.08	0.10	0.04	0.05	0.06	0.05	0.01	0.05	0.05
MgO	16.34	14.98	15.08	15.24	13.28	16.40	16.99	17.24	16.90	16.67	15.52	15.32	14.99	15.95	15.70	15.33	14.72	15.67	15.89	15.30
CaO	0.02	0.04	0.04	0.04	0.06	0.04	0.05	0.05	0.03	0.04	0.01	0.03	0.07	0.00	0.01	0.00	0.03	0.01	0.00	0.00
Na_2O	0.18	0.12	0.16	0.15	0.18	0.21	0.19	0.15	0.19	0.17	0.18	0.20	0.20	0.20	0.15	0.18	0.21	0.17	0.19	0.18
K_2O	8.94	8.14	8.12	8.60	7.96	9.00	8.91	8.43	9.01	9.14	9.12	8.97	8.92	8.75	8.76	8.62	8.45	8.57	8.54	8.60
F	1.60	1.48	1.25	1.25	1.20	1.36	1.11	1.21	1.18	1.29	1.07	1.04	0.92	0.69	0.65	0.64	0.57	0.66	0.70	0.74
Cl	0.13	0.13	0.14	0.16	0.14	0.17	0.15	0.13	0.17	0.18	0.20	0.19	0.16	0.16	0.16	0.14	0.18	0.19	0.15	0.17
Total	96.52	89.70	92.27	91.21	93.44	94.57	96.07	94.92	95.48	95.03	95.74	93.99	94.53	97.04	95.24	94.40	91.67	94.56	94.28	92.00
Structural formulae based on 22 oxygen atoms																				
Tetrahedral																				
^{IV}Si	5.89	5.76	5.83	5.65	5.79	5.75	5.75	5.70	5.74	5.69	5.55	5.56	5.61	5.84	5.81	5.79	5.75	5.87	5.87	5.81
^{IV}Al	2.54	2.59	2.53	2.44	2.85	2.37	2.42	2.35	2.30	2.34	2.48	2.48	2.49	2.49	2.56	2.52	2.77	2.48	2.52	2.49
Octahedral																				
^{VI}Al	0.20	0.19	0.22	0.00	0.50	0.00	0.05	0.00	0.00	0.00	0.00	0.00	0.00	0.24	0.28	0.22	0.44	0.27	0.30	0.20
Ti	0.31	0.27	0.29	0.37	0.35	0.35	0.34	0.35	0.38	0.39	0.45	0.44	0.41	0.37	0.32	0.36	0.29	0.34	0.28	0.32
Fe	1.38	1.67	1.69	1.82	1.66	1.64	1.57	1.68	1.65	1.67	1.87	1.86	1.90	1.57	1.60	1.64	1.54	1.56	1.54	1.63
Mn	0.01	0.01	0.01	0.01	0.01	0.01	0.01	0.01	0.01	0.01	0.01	0.01	0.01	0.01	0.01	0.01	0.01	0.00	0.01	0.01
Mg	3.53	3.53	3.45	3.58	2.98	3.69	3.73	3.85	3.76	3.74	3.48	3.50	3.40	3.44	3.46	3.42	3.36	3.47	3.52	3.50
ΣVI	*5.67*	*5.83*	*5.79*	*5.87*	*5.63*	*5.81*	*5.83*	*5.94*	*5.84*	*5.84*	*5.85*	*5.85*	*5.82*	*5.71*	*5.75*	*5.74*	*5.72*	*5.72*	*5.75*	*5.76*
K	1.66	1.64	1.59	1.73	1.53	1.73	1.68	1.61	1.71	1.75	1.75	1.75	1.73	1.62	1.65	1.64	1.65	1.62	1.62	1.69
Ca	0.00	0.01	0.01	0.01	0.01	0.01	0.01	0.01	0.00	0.01	0.00	0.01	0.01	0.00	0.00	0.00	0.01	0.00	0.00	0.00
Na	0.05	0.04	0.05	0.05	0.05	0.06	0.06	0.04	0.05	0.05	0.05	0.06	0.06	0.06	0.04	0.05	0.06	0.05	0.05	0.05
Σ Interlayer	*1.71*	*1.69*	*1.65*	*1.79*	*1.60*	*1.81*	*1.75*	*1.67*	*1.78*	*1.82*	*1.81*	*1.82*	*1.81*	*1.67*	*1.70*	*1.70*	*1.72*	*1.67*	*1.67*	*1.74*
F	0.72	0.74	0.60	0.61	0.56	0.64	0.51	0.56	0.55	0.61	0.50	0.50	0.50	0.31	0.30	0.30	0.27	0.30	0.32	0.35
Cl	0.03	0.04	0.04	0.04	0.04	0.04	0.04	0.03	0.06	0.05	0.07	0.05	0.05	0.04	0.04	0.04	0.05	0.05	0.04	0.04
X(Mg)	0.72	0.68	0.67	0.66	0.64	0.69	0.70	0.70	0.69	0.69	0.65	0.65	0.64	0.69	0.68	0.68	0.69	0.69	0.70	0.68
T (°C)	733	698	707	737	724	738	740	740	752	753	760	756	745	744	724	739	712	734	712	725
Fe/(Fe + Mg)	0.28	0.32	0.33	0.34	0.36	0.31	0.30	0.30	0.31	0.31	0.35	0.35	0.36	0.31	0.32	0.32	0.31	0.31	0.30	0.32

Table 1 (*continued*)

Sample no.	ALD-4	ALD-4	ALD-4	ALD-57	ALD-57	ALD-57	ALD-57	ALD-16	ALD-16	ALD-16	ALD-16	ALD-16	ALD-16	ALD-4	ALD-4	ALD-43	ALD-43	ALD-43	ALD-43	ALD-16	ALD-16	ALD-16	ALD-16
Depth (m)	477	477	477	672	672	672	672	142	142	142	142	142	142	477	477	730	730	730	730	142	142	142	142
	1	2	3	1	2	3	4	1	2	3	4	5	6	1	2	1	2	3	4	1	2	3	4
Lithology	Porph. 2	Porph. 2	Porph. 2	Porph. 4	Porph. 4	Porph. 4	Porph. 4	Porph. 4	Porph. 4	Porph. 4	Porph. 4	Porph. 4	Porph. 4	Porph. 2	Porph. 2	Porph. 4	Porph. 4	Porph. 4	Porph. 4	Porph. 4	Porph. 4	Porph. 4	Porph. 4
Alteration	Potas.	Potas.	Potas.	Potas.	Potas.	Potas.	Potas.	Potas.	Potas.	Potas.	Potas.	Potas.	Potas.	Potas.	Potas.	Potas.	Potas.	Potas.	Potas.	Potas.	Potas.	Potas.	Potas.
Origin	Mag.	Mag.	Mag.	Mag.	Mag.	Mag.	Mag.	Mag.	Mag.	Mag.	Mag.	Mag.	Mag.	Hyd.	Hyd.	Hyd.	Hyd.	Hyd.	Hyd.	Hyd.	Hyd.	Hyd.	Hyd.
SiO_2	36.53	37.21	37.20	39.09	38.60	39.99	39.90	36.72	36.90	37.12	37.25	37.29	37.42	37.53	37.55	38.66	38.48	38.72	40.37	38.48	38.63	39.03	39.29
TiO_2	3.48	3.27	3.32	3.78	4.30	3.06	3.25	3.47	3.06	3.33	3.37	3.18	3.24	3.29	3.69	2.56	2.84	2.91	1.71	2.50	2.74	2.42	2.42
Al_2O_3	14.61	14.42	14.82	15.79	15.35	14.63	14.70	14.65	14.72	14.60	14.30	14.65	14.70	13.87	15.45	13.42	13.50	13.67	14.91	14.16	13.98	13.62	13.76
^{t}FeO	11.53	11.58	11.06	8.79	9.50	7.87	7.65	11.13	10.01	10.45	10.42	10.43	10.50	10.51	11.52	5.21	5.37	5.35	6.21	9.61	9.53	9.41	9.12
MnO	0.09	0.11	0.03	0.31	0.33	0.30	0.30	0.02	-0.04	0.05	0.04	0.04	0.03	0.08	0.04	0.30	0.29	0.34	0.32	0.00	0.01	0.04	0.02
MgO	17.97	17.42	17.75	18.56	17.94	18.97	18.82	17.96	17.86	18.15	18.11	17.65	17.81	19.05	17.13	20.23	19.86	19.69	20.20	19.21	19.68	19.94	19.97
CaO	0.00	0.00	0.00	0.04	0.00	0.01	0.01	0.00	0.01	0.00	0.00	0.00	0.00	0.00	0.00	0.00	0.00	0.00	0.03	0.00	0.00	0.00	0.00
Na_2O	0.23	0.19	0.18	0.16	0.21	0.20	0.15	0.33	0.25	0.41	0.37	0.33	0.23	0.23	0.23	0.21	0.20	0.22	0.18	0.28	0.09	0.17	0.17
K_2O	8.96	9.02	9.18	9.85	9.61	10.02	9.91	8.90	9.11	9.00	9.13	9.13	9.13	9.25	9.09	8.60	8.59	8.66	9.95	9.42	9.33	9.53	9.20
F	1.70	1.59	1.54	1.94	1.77	1.52	1.74	1.81	1.57	1.78	2.02	1.78	1.76	1.25	1.35	2.94	3.14	2.98	1.99	2.56	2.32	2.60	2.94
Cl	0.20	0.20	0.20	0.11	0.11	0.11	0.09	0.14	0.13	0.15	0.14	0.14	0.16	0.18	0.19	0.11	0.08	0.09	0.12	0.12	0.13	0.14	0.12
Total	95.27	94.96	95.28	97.57	96.95	96.03	95.75	95.14	93.59	95.02	95.14	94.62	94.98	95.24	96.26	92.22	92.35	92.63	95.99	96.32	96.38	96.89	96.98
Structural formulae based on 22 oxygen atoms																							
Tetrahedral																							
^{IV}Si	5.48	5.59	5.55	5.60	5.58	5.78	5.78	5.51	5.58	5.55	5.58	5.60	5.60	5.58	5.54	5.85	5.83	5.84	5.85	5.69	5.69	5.74	5.76
^{IV}Al	2.59	2.55	2.61	2.67	2.62	2.49	2.51	2.59	2.62	2.57	2.53	2.59	2.59	2.43	2.69	2.39	2.41	2.43	2.55	2.47	2.42	2.36	2.38
Octahedral																							
^{VI}Al	0.52	0.41	0.45	0.10	0.05	0.10	0.10	0.49	0.42	0.45	0.44	0.40	0.40	0.42	0.46	0.00	0.00	0.00	0.20	0.31	0.31	0.26	0.24
Ti	0.39	0.37	0.37	0.41	0.47	0.33	0.35	0.39	0.35	0.37	0.38	0.36	0.36	0.37	0.41	0.29	0.32	0.33	0.19	0.28	0.30	0.27	0.27
Fe	1.45	1.45	1.38	1.05	1.15	0.95	0.93	1.40	1.27	1.31	1.31	1.31	1.31	1.31	1.42	0.66	0.68	0.68	0.75	1.19	1.17	1.16	1.12
Mn	0.01	0.01	0.00	0.04	0.04	0.04	0.04	0.00	0.00	0.01	0.01	0.00	0.00	0.01	0.01	0.04	0.04	0.04	0.04	0.00	0.00	0.00	0.00
Mg	4.02	3.90	3.95	3.96	3.87	4.09	4.06	4.02	4.03	4.05	4.05	3.95	3.97	4.22	3.77	4.56	4.49	4.43	4.36	4.24	4.32	4.37	4.37
ΣVI	*5.94*	*5.88*	*5.87*	*5.73*	*5.73*	*5.68*	*5.67*	*5.91*	*5.84*	*5.87*	*5.85*	*5.82*	*5.84*	*5.92*	*5.82*	*5.80*	*5.78*	*5.75*	*5.74*	*5.87*	*5.91*	*5.90*	*5.90*
K	1.72	1.73	1.75	1.80	1.77	1.85	1.83	1.70	1.76	1.72	1.75	1.75	1.74	1.76	1.71	1.66	1.66	1.67	1.84	1.78	1.75	1.79	1.72
Ca	0.00	0.00	0.00	0.01	0.00	0.00	0.00	0.00	0.00	0.00	0.00	0.00	0.00	0.00	0.00	0.00	0.00	0.00	0.01	0.00	0.00	0.00	0.00
Na	0.07	0.06	0.05	0.04	0.06	0.06	0.04	0.10	0.07	0.12	0.11	0.10	0.07	0.07	0.06	0.06	0.06	0.06	0.05	0.08	0.03	0.05	0.05
Σ Interlayer	*1.78*	*1.78*	*1.80*	*1.86*	*1.83*	*1.91*	*1.88*	*1.80*	*1.83*	*1.84*	*1.85*	*1.85*	*1.81*	*1.82*	*1.77*	*1.72*	*1.72*	*1.73*	*1.90*	*1.86*	*1.78*	*1.83*	*1.77*
F	0.79	0.74	0.74	0.86	0.79	0.68	0.78	0.85	0.74	0.83	0.94	0.83	0.83	0.58	0.62	1.35	1.45	1.40	0.89	1.17	1.05	1.18	1.32
Cl	0.05	0.05	0.05	0.05	0.03	0.03	0.02	0.04	0.04	0.03	0.03	0.03	0.04	0.05	0.05	0.05	0.02	0.03	0.03	0.03	0.03	0.03	0.03
X(Mg)	0.74	0.73	0.74	0.79	0.77	0.81	0.81	0.74	0.76	0.76	0.76	0.75	0.75	0.76	0.73	0.87	0.87	0.87	0.85	0.78	0.79	0.79	0.80
T (°C)	769	759	764	793	801	777	786	771	763	770	772	763	765	771	771	789	798	800	722	743	756	741	744
Fe/(Fe+Mg)	0.26	0.27	0.26	0.21	0.23	0.19	0.19	0.26	0.24	0.24	0.24	0.25	0.25	0.24	0.27	0.13	0.13	0.13	0.15	0.22	0.21	0.21	0.20

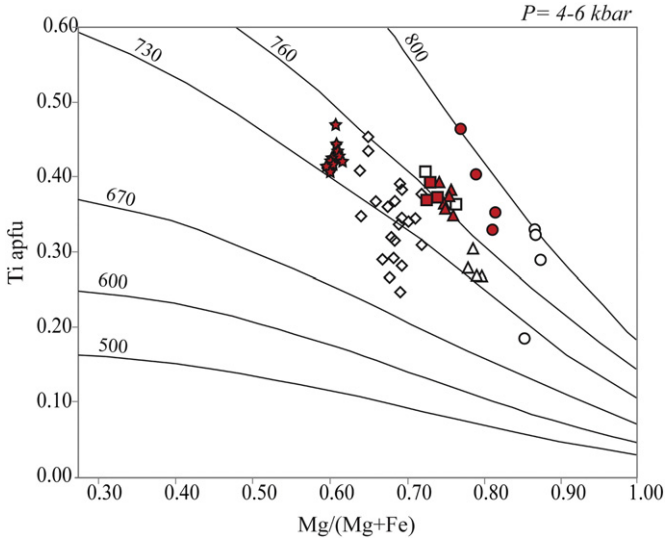

Fig. 7. Concentration of Ti (apfu = atoms/formula unit) and Mg mole fraction (X_{Mg} = molar Mg/(Mg + Fe) in biotite are plotted relative to isotherms from the geothermometer of Henry et al. (2005).

quantity or is rarely present. A relict mineral that is not stable in the association is given in parentheses after the mineral that replaces it. When a group of minerals characteristic of certain alteration assemblage are not necessarily contemporaneous, they are separated by commas.

Representative samples (n = 90) of the different pulses of alteration and mineralization were selected for X-ray and electron microprobe analysis. Most of the samples selected belong to profile 6516700 N that contains the highest copper grades in the project and reached the deepest levels in the system (Fig. 3). Samples from the profiles located north (6517000 N) and south (6516600 N) and from the epithermal Au-Ag-Cu veins that crop out on the high ridges of the project were also analyzed. In each sample studied by X-ray diffraction the total fraction and the oriented aggregates <2 um were analyzed using a Cu-Kα radiation and X-ray diffraction traces at 40 kV and 20 mA. 30 g of crushed whole rock sample were disaggregated and dispersed with ultrasound in one liter of distilled water. For the preparation of the oriented aggregates, the samples were homogenized and the fraction <2 mm was extracted with $SrCl_2$, dried at ambient temperature (air dried), subjected to vapors of ethylene and calcined at 375 °C and 550 °C. Illite was identified by X ray diffraction in the <2 μm fraction and distinguished in air-dried, ethylene glycol-saturated, and calcinated samples by the sharp reflection of the 001 peak at 10 Å, and by rational 2nd, 3rd, and 4th order reflections. To determine the varieties of chlorite and illite polytypes, the fraction <1 μm was extracted from the disaggregated samples by ultracentrifugation and analyzed by the scanning mode in steps (0.02° per step) from 16° to 44° 2θ. The X-ray diffraction reflections were evaluated with the Rigaku software. Quantitative analyzes of the clays were performed following the Mineral Intensity Factor method described by Moore and Reynolds (1997). For quantitative estimation of phyllosilicatesNEWMOD program was used.

Biotite and chlorite compositions (n = 77) were determined by electron probe micro-analysis (EPMA) at the microanalytical facility at the University of New Brunswick (Canada); mineral compositions were determined in wavelength-dispersion mode on a JXA JEOL-733 Superprobe, with 15 kV accelerating voltage, 10 nA beam current, and a maximum 40 s counting interval. Mica, illite, and kaolinite microprobe analyses (n = 99) were carried out at the Electron

Table 2
Representative microprobe analyses of hydrothermal chlorite from different alteration and clay zones in the Altar porphyry Cu deposit.

Sample n°	ALD-49	ALD-49	ALD-49	ALD-49	ALD-49	ALD-49	ALD-49	ALD-49	ALD-49	ALD-49
Depth (m)	77	77	77	77	77	77	77	77	77	77
Analyses	1	2	3	4	5	6	7	8	9	10
Lithology	Porph. 4	Porph. 4	Porph. 4	Porph. 4	Porph. 4	Porph. 4	Porph. 4	Porph. 4	Porph. 4	Porph. 4
Alteration	Prop.	Prop.	Prop.	Prop.	Prop.	Prop.	Prop.	Prop.	Prop.	Prop.
SiO_2	28.53	28.47	28.07	28.99	27.89	28.77	27.95	28.02	28.96	27.47
TiO_2	0.06	0.05	0.05	0.08	0.05	0.04	0.05	0.05	0.04	0.04
Al_2O_3	20.65	20.26	20.45	19.91	20.84	20.75	21.51	21.57	20.97	21.24
^{1}FeO	20.50	20.12	20.33	19.45	19.50	20.38	20.58	21.68	19.86	21.69
MnO	0.35	0.30	0.32	0.32	0.34	0.38	0.32	0.32	0.32	0.30
MgO	19.00	18.65	18.80	18.58	18.71	18.50	19.09	18.92	18.40	19.01
CaO	0.03	0.05	0.04	0.06	0.07	0.10	0.04	0.04	0.13	0.03
Na_2O	0.02	0.02	0.01	0.04	0.01	0.02	0.03	0.01	0.02	0.02
K_2O	0.04	0.10	0.07	0.10	0.10	0.08	0.06	0.04	0.11	0.04
F	0.00	0.00	0.00	0.00	0.00	0.00	0.00	0.00	0.00	0.00
Cl	0.01	0.01	0.01	0.00	0.01	0.00	0.01	0.01	0.01	0.00
Total	89.24	88.10	88.20	87.60	87.63	89.08	89.69	90.70	88.92	89.85
Structural formulae based on $O_{20}(OH)_{16}$										
Cations										
Si	5.67	5.78	5.70	5.89	5.69	5.78	5.59	5.57	5.81	5.52
^{IV}Al	2.33	2.22	2.30	2.11	2.31	2.22	2.41	2.43	2.19	2.48
^{VI}Al	2.50	2.63	2.60	2.66	2.69	2.69	2.66	2.62	2.77	2.55
Ti	0.01	0.01	0.01	0.01	0.01	0.01	0.01	0.01	0.01	0.01
Fe^{2+}	3.40	3.42	3.45	3.31	3.32	3.42	3.44	3.60	3.33	3.64
Mn	0.06	0.06	0.06	0.06	0.06	0.06	0.05	0.05	0.05	0.05
Mg	5.92	5.65	5.70	5.63	5.69	5.54	5.69	5.60	5.50	5.69
Σ Oct.	11.89	11.76	11.82	11.67	11.77	11.72	11.85	11.88	11.66	11.94
K	0.01	0.01	0.01	0.01	0.02	0.02	0.01	0.01	0.03	0.01
Ca	0.01	0.02	0.00	0.02	0.00	0.01	0.01	0.00	0.01	0.01
Na	0.01	0.03	0.02	0.03	0.03	0.02	0.02	0.01	0.03	0.01
Σ Intercapa	0.03	0.05	0.03	0.05	0.05	0.05	0.04	0.02	0.06	0.02
$Fe^{+2}/(Fe^{+2} + Mg^{+2})$	0.37	0.38	0.38	0.37	0.37	0.38	0.38	0.39	0.38	0.39
^{2}T (°C)	314	295	308	277	311	296	326	330	291	337

Microprobe Laboratory, College of Earth, Ocean and Atmospheric Sciences, Oregon State University, USA. These analyses were performed with a Cameca SX-100 Electron Microprobe equipped with five wavelength dispersive spectrometers (WDS) and one energy dispersive spectrometer (EDS) with a thin window for light element detection. Operating conditions were 15 kV and 30 nA with a beam diameter of 5 μm.

Mid-infrared (MIR) spectra of clay material were acquired on KBr pellets using a Nicolet 760 FT-IR spectrometer form the Universite de Poitiers equipped with a potassium bromide (KBr) beam splitter and DTGSKBr detector. The resolution was set at 4 cm^{-1} with co-addition of 100 scans. KBr pellets contained 1 mg of sample for 150 mg of KBr powder, were crushed into a mortar and pressed under 8 tons for 5 min in a hydraulic press before drying at 120 °C.

We used the empirical X_{Mg}-Ti in biotite geothermometer of Henry et al. (2005) to calculate the temperatures of igneous and hydrothermal biotite. This geothermometer has been recently used with success on the porphyry system of Butte, Montana (Mercer and Reed, 2013). Errors arising from application of the biotite geothermometer are related to microprobe analytical uncertainties. Precision of the geothermometer is estimated to be ±24 °C in the 480° to 700 °C range and ±12 °C in the 700° to 800 °C range (Henry et al., 2005).

5. Results

Fig. 2A and B show the lateral distribution of the phyllosilicates at surface along with the contour of the porphyritic stocks and the distribution of copper grades. Fig. 3 presents the distribution of phyllosilicates in the section 6516700 mN that contains the deepest drill holes and intersects the best explored mineralized zone of Altar Central.

5.1. Biotite

Using petrographic techniques, the studied biotite-bearing assemblages were divided into magmatic and hydrothermal types. The term magmatic refers to biotite crystallized directly from a silicate melt and occur as euhedral to subhedral phenocrysts that range in size from 0.5 mm to 1 cm (Fig. 4). The hydrothermal biotite is petrographically distinct from the magmatic type, occurring in the potassic altered rocks as randomly oriented aggregates of fine-grained flakes (Fig. 4).

Magmatic biotites from porphyry 2 and porphyry 4 with potassic alteration have a light-brown color (0.4 mm–1 cm) indicating they are intermediate between oxidized and reduced (cf. Lalonde and Bernard, 1993) and contain inclusions of apatite needles (Fig. 4A). The structural formula of biotite from analyses (Table 1) was recalculated for 22 oxygen atoms (Table 1; Moore and Reynolds, 1997). Representative magmatic biotite crystals from porphyry 2 (Table 1) have the compositional range $K_{1.75–1.72}$ $Na_{0.07–0.05}$ $Ca_{0.00}$ $(Al_{0.5–0.4}$ $Mg_{4.02–3.90}$ $Fe_{1.45–1.38}$ $Ti_{0.39–0.37}$ $Mn_{0.01–0.00})$ $(Si_{5.59–5.48}$ $Al_{2.61–2.55})$ O_{10} $(OHF_{0.79–0.74}Cl_{0.05})_4$. Representative magmatic biotite crystals from porphyry 4 (Table 1) have the compositional range $K_{1.85–1.70}$ $Na_{0.12–0.07}$ $Ca_{0.01–0.00}$ $(Al_{0.4–0.5}$ $Mg_{4.09–3.95}$ $Fe_{1.4–1.27}$ $Ti_{0.47–0.35}$ $Mn_{0.04–0.00})$ $(Si_{5.78–5.51}$ $Al_{2.67–2.53})$ O_{10} $(OHF_{0.94–0.74}$ $Cl_{0.05–0.03})_4$.

Magmatic biotites from the barren dacite porphyry have reddish-brown color (reduced, cf. Lalonde and Bernard, 1993) and range in size from 0.2 mm to 1.2 mm (Fig. 4B). Representative magmatic biotite crystals from this intrusion (Table 1) have the compositional range $K_{1.74–1.53}$ $Na_{0.32–0.21}$ $Ca_{0.01–0.00}$ $(Al_{0.18–0.00}$ $Mg_{3.36–3.05}$ $Fe_{2.14–1.94}$ $Ti_{0.47–0.41}$ $Mn_{0.03–0.00})$ $(Si_{5.64–5.53}$ $Al_{2.55–2.41})$ O_{10} $(OHF_{0.26–0.13}$ $Cl_{0.04–0.03})_4$.

K is by far the dominant cation in the interlayer of the magmatic biotites, with minor Na and traces of Ca. Magnesium predominates over Fe (arbitrarily considered as Fe^{2+}) in the octahedral site, which is filled by small amounts of Ti, Al, and Mn^{2+}. The magmatic biotite

ALD-19	ALD-19	ALD-19	ALD-19	ALD-19	ALD-19	ALD-19	ALD-46	ALD-46	ALD-46
250	250	250	250	250	250	250	397	397	397
1	2	3	4	5	6	7	1	2	1
Porph. 4	Porph. 4	Porph. 4	Porph. 4	Porph. 4	Porph. 4	Porph. 4	Andesite	Andesite	Andesite
Chl.	Chl.	Chl.	Chl.	Chl.	Chl.	Chl.	Potas, Chl.	Potas, Chl.	Potas, Chl.
28.79	28.47	29.02	28.58	29.11	28.81	28.58	27.07	26.82	28.13
0.06	0.04	0.00	0.42	0.04	0.19	0.01	0.20	0.03	0.08
20.80	20.95	20.87	20.61	21.06	19.58	24.34	19.33	20.65	19.02
12.39	12.61	12.10	12.96	11.95	13.93	14.78	16.96	17.13	16.66
0.09	0.13	0.02	0.15	0.07	0.12	0.12	0.12	0.09	0.14
25.35	24.71	24.63	24.43	24.42	24.06	19.35	20.78	21.15	22.34
0.04	0.02	0.02	0.03	0.00	0.02	0.07	0.09	0.03	0.05
0.03	0.03	0.00	0.02	0.00	0.04	0.08	0.06	0.02	0.05
0.00	0.02	0.03	0.04	0.01	0.02	0.34	0.02	0.00	0.02
0.43	0.45	0.69	0.57	0.45	0.62	0.24	0.23	0.24	0.20
0.00	0.00	0.01	0.00	0.01	0.02	0.02	0.01	0.00	0.00
87.98	87.41	87.38	87.80	87.12	87.40	87.92	84.86	86.17	86.71
Structural formulae based on $O_{20}(OH)_{16}$									
Cations									
5.65	5.62	5.72	5.64	5.67	6.03	5.64	5.66	5.51	5.73
2.35	2.38	2.28	2.36	2.33	1.97	2.36	2.34	2.49	2.27
2.46	2.50	2.56	2.44	2.71	2.86	3.29	2.42	2.50	2.29
0.01	0.01	0.00	0.06	0.01	0.03	0.00	0.03	0.00	0.01
2.03	2.08	1.99	2.14	1.95	2.44	2.44	2.96	2.94	2.84
0.01	0.02	0.00	0.03	0.01	0.02	0.02	0.02	0.02	0.02
7.41	7.28	7.24	7.19	7.09	6.11	5.69	6.48	6.47	6.78
11.93	11.89	11.80	11.85	11.76	11.46	11.44	11.91	11.94	11.95
0.00	0.01	0.01	0.01	0.01	0.01	0.09	0.02	0.00	0.01
0.00	0.00	0.00	0.00	0.00	0.00	0.01	0.01	0.01	0.01
0.01	0.01	0.00	0.00	0.00	0.02	0.03	0.00	0.10	0.02
0.02	0.06	0.06	0.06	0.05	0.08	0.15	0.03	0.10	0.04
0.22	0.22	0.22	0.23	0.22	0.25	0.30	0.31	0.31	0.29
317	321	305	318	314	260	319	315	340	304

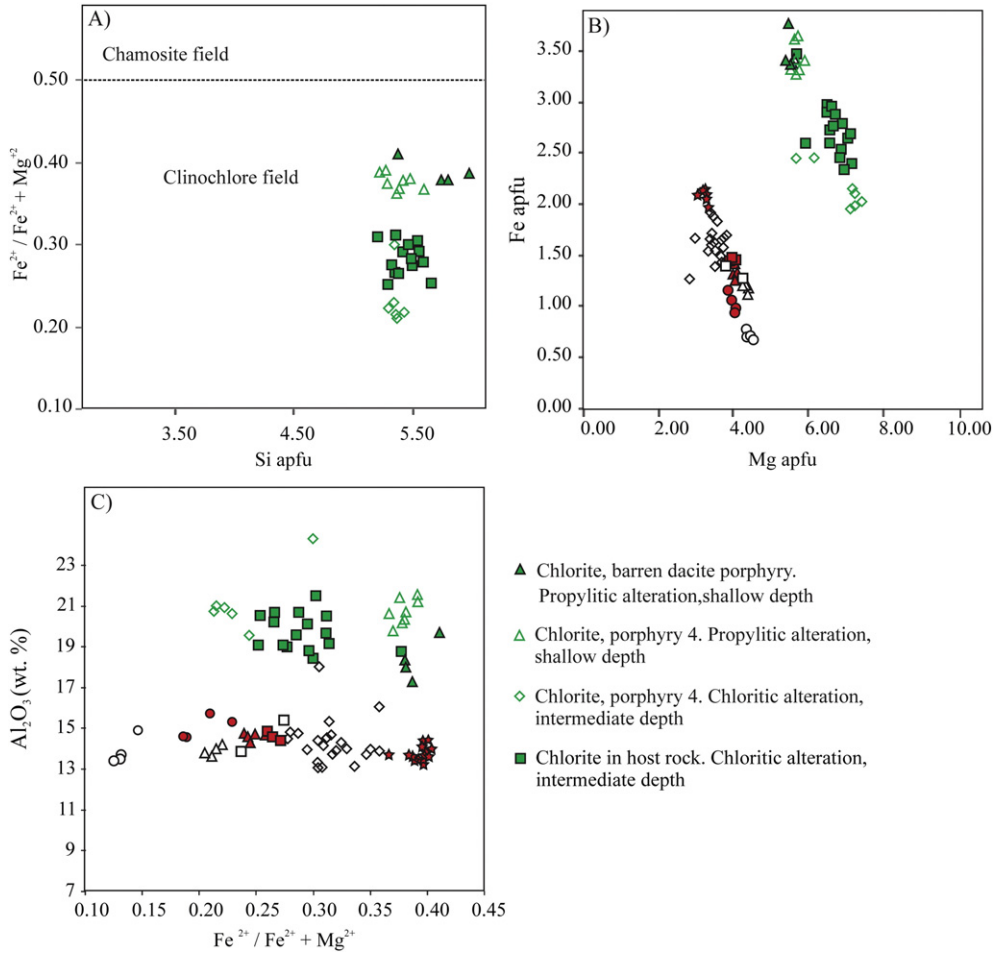

Fig. 8. Compositions of chlorites. A) Fe/(Fe + Mg) vs Si (apfu), B) Fe versus Mg (apfu), C) Al_2O_3 (wt.%) versus Fe/(Fe + Mg)

from porphyry 4 plots in the phlogopite field (Fig. 5, Foster, 1962; Reider et al., 1999). Magmatic biotites from the barren dacite porphyry plot in the Mg-biotite field, whereas magmatic biotites from porphyry 2 have intermediate compositions between phlogopite and Mg-biotite (Fig. 5). In the diagram of $Fe^{2+}/(Fe^{2+} + Mg)$ versus Al^{IV} content, magmatic biotites from porphyries 2 and 4 plot in the phlogopite field and biotite from the barren dacite porphyry plot in the biotite field (Fig. 6A). The X_{Mg} in magmatic biotite increases from the barren dacite porphyry to porphyry 2 to porphyry 4, as does K and F contents (Fig. 6). Magmatic biotite analyses from a sample of the porphyry 4 obtained at 672 m depth have higher X_{Mg}, K, and lower Cl contents than magmatic biotite from a sample of porphyry 4 obtained at 142 m depth.

Biotite ± quartz ± anhydrite ± K feldspar ± albite ± rutile of the potassic alteration occurs as patches at shallow and intermediate levels affecting the porphyries and the wall rocks and is massive at depth (Fig. 3). Secondary biotite occurs as aggregates of very fine light-brownish plates (0.1–0.2 mm) replacing previous igneous ferromagnesian silicates (biotite and edenite, Fig. 4C). Hydrothermal biotite has apatite inclusions, and is associated with chalcopyrite, hematite, and rutile crystals. Representative hydrothermal biotite crystals in the porphyries (Table 1) have the compositional range $K_{1.84–1.66}$ $Na_{0.08–0.03}$ $Ca_{0.01–0.00}$ $(Al_{0.46–0.00}$ $Mg_{4.56–3.77}$ $Fe_{1.42–0.66}$ $Ti_{0.41–0.19}$ $Mn_{0.04–0.00})$ $(Si_{5.85–5.54}$ $Al_{2.69–2.36})$ O_{10} $(OH)_4$. Representative hydrothermal biotite crystals in the andesitic wall rocks (Table 1) have the compositional range $K_{1.75–1.48}$ $Na_{0.18–0.04}$ $Ca_{0.03–0.00}$ $(Al_{0.80–0.00}$ $Mg_{3.85–2.85}$ $Fe_{1.90–1.26}$ $Ti_{0.45–0.25}$ $Mn_{0.02–0.00})$ $(Si_{6.00–5.55}$ $Al_{3.00–2.30})$ O_{10} $(OH)_4$. According to Figs. 5 and 6, chemical analysis of hydrothermal biotites from porphyry 2 and 4 correspond to phlogopite and the hydrothermal biotites from

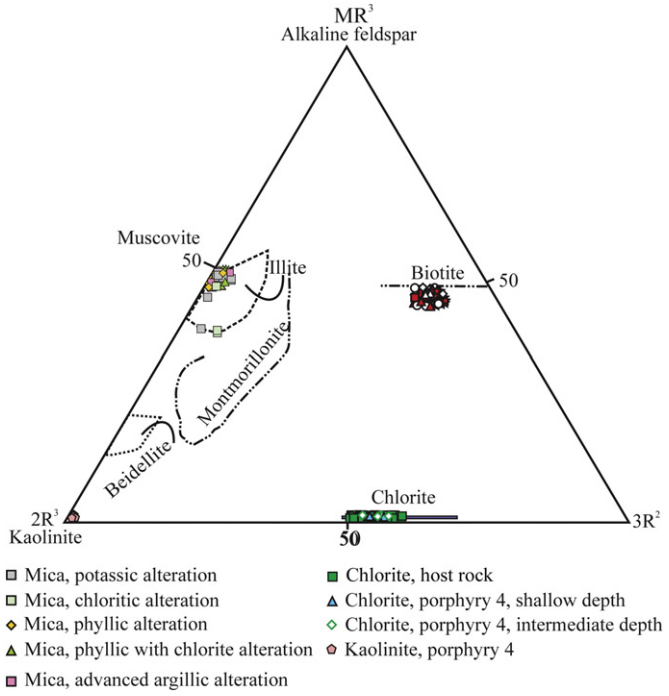

Fig. 9. Compositions of phyllosilicates at Altar where MR3 = Na + K + 2Ca; 2R3 = (Al + Fe^{3+}) − MR3) / 2 and 3R2 = (Mg + Mn + Fe^{2+}) / 3 (Velde, 1985). Composition range of common phyllosilicates is indicated for comparison (Velde, 1985; Newman and Brown, 1987).

Table 3
Representative Microprobe Analyses of Hydrothermal Potassic Dioctahedral Phyllosilicates from Different Alteration and Clay Zones in the Altar Porphyry Cu Deposit.

Drill hole	ALD-19	ALD-19	ALD-19	ALD-19	ALD-16	ALD-16	ALD-16	ALD-16	ALD-16	ALD-16	ALD-43	ALD-43	ALD-43	ALD-43	ALD-43	ALD-43	ALD-43	ALD-43	ALD-43	ALD-43
Depth (m)	250	250	250	250	101	101	101	101	101	101	788	788	788	788	788	263	263	263	263	263
	1	2	3	4	1	2	3	4	5	6	1	2	3	4	5	1	2	3	4	5
Alteration	Chl.	Chl.	Chl.	Chl.	Phy.	Phy.	Phy.	Phy.	Phy.	Phy.	Phy.	Phy.	Phy.	Phy.	Phy.	Phy.	Phy.	Phy.	Phy.	Phy.
Lithologie	Porph. 4	Porph. 4	Porph. 4	Porph. 4	Porph. 4	Porph. 4	Porph. 4	Porph. 4	Porph. 4	Porph. 4	Porph. 4	Porph. 4	Porph. 4	Porph. 4	Porph. 4	Porph. 4	Porph. 4	Porph. 4	Porph. 4	Porph. 4
(wt%)																				
SiO_2	47.53	47.98	47.80	47.28	49.23	51.99	49.70	49.76	49.77	47.68	46.36	46.25	46.44	46.65	45.95	48.34	46.83	48.92	47.46	48.07
TiO_2	0.05	0.00	0.00	0.05	0.10	0.23	0.01	0.04	0.06	0.12	0.11	0.29	0.32	0.39	0.37	1.29	0.54	0.43	0.12	0.17
Al_2O_3	31.62	29.71	33.16	29.92	34.50	36.11	35.81	33.64	35.42	33.35	33.30	34.08	33.60	34.45	35.58	33.21	33.95	32.71	35.64	35.99
[1]FeO	1.25	2.57	2.46	2.42	0.89	0.66	0.43	0.22	0.02	2.01	1.30	1.30	1.31	1.33	1.14	1.33	1.41	1.46	0.77	1.07
MnO	0.04	0.04	0.02	0.02	0.01	0.01	0.00	0.02	0.02	0.00	0.01	0.01	0.01	0.00	0.00	0.00	0.01	0.01	0.02	0.00
MgO	1.12	3.83	1.73	4.79	0.65	0.66	0.52	0.23	0.19	0.93	3.12	2.22	2.59	1.99	1.16	1.06	0.81	1.02	0.78	0.76
CaO	0.13	0.27	0.02	0.36	0.08	0.11	0.12	0.19	0.15	0.12	0.01	0.01	0.00	0.00	0.01	0.02	0.02	0.04	0.01	0.00
Na_2O	0.41	0.63	0.51	0.10	0.50	0.31	0.31	0.43	0.43	0.31	0.43	0.54	0.49	0.47	0.53	0.85	1.14	1.06	1.82	1.54
K_2O	8.90	5.95	8.52	6.28	9.12	9.30	9.31	8.37	8.73	9.96	10.10	10.76	10.35	10.45	10.38	8.37	8.82	8.21	7.87	8.41
F	0.30	0.40	0.16	0.54	0.23	0.00	0.13	0.14	0.00	0.23	n.a	n.a	n.a	n.a	n.a	n.a	n.a	n.a	n.a	n.a
Cl	0.03	0.02	0.00	0.02	0.00	0.02	0.00	0.02	0.01	0.00	0.02	0.02	0.01	0.01	0.01	0.07	0.01	0.01	0.01	0.01
SO_2	n.a	n.a	n.a	n.a	n.a	n.a	n.a	n.a	n.a	n.a	0.04	0.04	0.02	0.04	0.09	0.06	0.02	0.02	0.06	0.01
P_2O_5	n.a	n.a	n.a	n.a	n.a	n.a	n.a	n.a	n.a	n.a	0.03	0.02	0.01	0.02	0.01	0.04	0.03	0.04	0.00	0.01
SrO	n.a	n.a	n.a	n.a	n.a	n.a	n.a	n.a	n.a	n.a	0.00	0.00	0.01	0.00	0.00	0.00	0.00	0.00	0.00	0.00
Total	91.38	91.40	94.39	91.78	95.32	99.38	96.36	93.05	94.80	94.70	94.73	95.44	95.12	95.73	95.12	94.62	93.58	93.91	94.57	96.03
Structural formulae based on 22 Oxygen atoms																				
[IV]Si	6.53	6.55	6.38	6.45	6.46	6.50	6.42	6.61	6.49	6.38	6.21	6.17	6.20	6.18	6.12	6.40	6.30	6.51	6.26	6.26
[IV]Al	1.47	1.45	1.62	1.55	1.54	1.50	1.58	1.39	1.51	1.62	1.79	1.83	1.80	1.82	1.88	1.60	1.70	1.49	1.74	1.74
Octahedral																				
[VI]Al	3.66	3.33	3.60	3.25	3.79	3.82	3.88	3.88	3.93	3.65	3.46	3.52	3.49	3.56	3.70	3.58	3.68	3.64	3.80	3.79
Ti	0.01	0.00	0.00	0.00	0.01	0.02	0.00	0.00	0.01	0.01	0.01	0.03	0.03	0.04	0.04	0.13	0.05	0.04	0.01	0.02
Fe	0.14	0.29	0.27	0.28	0.10	0.07	0.05	0.02	0.00	0.22	0.15	0.14	0.15	0.15	0.13	0.15	0.16	0.16	0.09	0.12
Mn	0.00	0.00	0.00	0.00	0.00	0.00	0.00	0.00	0.00	0.00	0.00	0.00	0.00	0.00	0.00	0.00	0.00	0.00	0.00	0.00
Mg	0.23	0.78	0.34	0.97	0.13	0.12	0.10	0.05	0.04	0.19	0.62	0.44	0.52	0.39	0.23	0.21	0.16	0.20	0.15	0.15
SVI	*4.04*	*4.41*	*4.22*	*4.51*	*4.03*	*4.03*	*4.03*	*3.96*	*3.98*	*4.07*	*4.24*	*4.14*	*4.18*	*4.14*	*4.10*	*4.06*	*4.05*	*4.05*	*4.06*	*4.07*
Ca	0.02	0.04	0.00	0.05	0.01	0.01	0.02	0.03	0.02	0.02	0.00	0.00	0.00	0.00	0.00	0.00	0.00	0.01	0.00	0.00
Na	0.11	0.17	0.13	0.03	0.13	0.08	0.08	0.11	0.11	0.08	0.11	0.14	0.13	0.12	0.14	0.22	0.30	0.27	0.47	0.39
K	1.56	1.04	1.45	1.09	1.53	1.48	1.53	1.42	1.45	1.70	1.72	1.83	1.76	1.77	1.76	1.41	1.51	1.39	1.32	1.40
Sr	0.00	0.00	0.00	0.00	0.00	0.00	0.00	0.00	0.00	0.00	0.00	0.00	0.00	0.00	0.00	0.00	0.00	0.00	0.00	0.00
ΣInterlayer	*1.69*	*1.24*	*1.59*	*1.17*	*1.67*	*1.57*	*1.63*	*1.56*	*1.58*	*1.80*	*1.84*	*1.97*	*1.89*	*1.89*	*1.90*	*1.63*	*1.81*	*1.67*	*1.79*	*1.79*
F	0.13	0.17	0.07	0.23	0.10	0.00	0.05	0.06	0.00	0.10	0.00	0.00	0.00	0.00	0.00	0.00	0.00	0.00	0.00	0.00
Cl	0.01	0.00	0.00	0.00	0.00	0.00	0.00	0.00	0.00	0.00	0.00	0.00	0.00	0.00	0.00	0.01	0.00	0.00	0.00	0.00
Si/Al	1.28	1.37	1.22	1.34	1.21	1.22	1.18	1.26	1.19	1.21	1.18	1.15	1.17	1.15	1.10	1.23	1.17	1.27	1.13	1.13

1. All iron as Fe^{2+} SVI: sum. of octahedral cations.
Abbreviations: AA: advanced argillic; Barren dac: barren dacite porphyry; Chl: chloritic; Hyd: hydrothermal; Mag: magmatic; Porph: porphyry; Potas: potassic; Pyroclas: Pyroclastic rock.

Table 3 (*continued*)

Drill hole	ALD-43	ALD-43	ALD-43	ALD-43	ALD-43	ALD-43	ALD-43	ALD-43	ALD-43	ALD-43	ALD-43	ALD-43	ALD-43	ALD-43	ALD-43	ALD-43	ALD-43	ALD-43	ALD-43	ALD-57
Depth (m)	263	263	263	263	263	263	263	263	263	263	263	263	263	263	263	263	263	263	263	366
	6	7	8	9	10	11	12	13	14	15	16	17	18	19	20	21	22	23	24	1
Alteration	Phy.	Phy.	Phy.	Phy.	Phy.	Phy.	Phy.	Phy.	Phy.	Phy.	Phy.	Phy.	Phy.	Phy.	Phy.	Phy.	Phy.	Phy.	Phy.	Phy.
Lithologie	Porph. 4	Porph. 4	Porph. 4	Porph. 4	Porph. 4	Porph. 4	Porph. 4	Porph. 4	Porph. 4	Porph. 4	Porph. 4	Porph. 4	Porph. 4	Porph. 4	Porph. 4	Porph. 4	Porph. 4	Porph. 4	Porph. 4	Andesite
(wt%)																				
SiO_2	47.28	46.40	47.59	46.98	46.15	47.66	46.32	48.96	46.97	48.36	44.15	44.84	47.91	47.68	47.67	46.45	47.55	45.30	47.91	45.17
TiO_2	0.87	0.15	0.20	0.42	0.54	0.34	0.29	0.13	0.05	0.06	0.06	0.26	0.26	0.27	0.05	0.13	0.10	0.10	0.09	0.35
Al_2O_3	36.32	35.35	36.58	34.77	34.60	35.18	33.32	37.12	36.16	36.68	32.91	33.76	35.16	35.12	35.54	35.80	36.32	36.04	34.02	31.89
^{1}FeO	0.48	0.82	0.62	2.27	2.72	2.78	2.24	1.09	0.72	0.73	0.50	1.53	1.52	1.40	0.50	0.99	0.83	1.09	0.66	3.93
MnO	0.00	0.03	0.01	0.00	0.00	0.02	0.00	0.00	0.01	0.01	0.00	0.00	0.00	0.01	0.00	0.00	0.03	0.02	0.04	0.01
MgO	0.45	0.84	0.61	1.06	1.21	1.21	1.45	0.84	0.76	0.54	0.57	0.76	0.81	0.76	0.81	0.85	0.65	0.74	1.40	2.48
CaO	0.00	0.00	0.01	0.01	0.03	0.03	0.02	0.02	0.03	0.03	0.03	0.03	0.04	0.03	0.02	0.04	0.05	0.04	0.05	0.03
Na_2O	2.31	1.59	2.27	0.87	0.86	0.48	0.89	1.91	2.66	2.68	1.53	1.10	1.25	1.15	1.78	1.48	1.56	1.59	1.01	0.42
K_2O	6.98	8.02	7.27	9.27	9.73	8.19	9.04	7.95	6.55	6.56	6.84	8.61	8.39	8.36	7.23	7.90	7.74	8.52	8.63	9.78
F	n.a	n.a	n.a	n.a	n.a	n.a	n.a	n.a	n.a	n.a	n.a	n.a	n.a	n.a	n.a	n.a	n.a	n.a	n.a	n.a
Cl	0.01	0.01	0.01	0.02	0.02	0.02	0.03	0.01	0.04	0.01	0.12	0.06	0.02	0.02	0.03	0.01	0.02	0.02	0.03	0.03
SO_2	0.05	0.09	0.04	0.02	0.03	0.01	0.05	0.06	0.05	0.04	0.15	0.06	0.02	0.04	0.04	0.03	0.06	0.03	0.03	0.05
P_2O_5	0.01	0.02	0.03	0.02	0.04	0.02	0.03	0.02	0.02	0.00	0.01	0.04	0.04	0.10	0.01	0.03	0.02	0.03	0.01	0.01
SrO	0.00	0.00	0.01	0.00	0.00	0.00	0.00	0.00	0.00	0.00	0.00	0.00	0.00	0.00	0.00	0.02	0.00	0.00	0.00	0.00
Total	94.76	93.31	95.25	95.70	95.93	95.95	93.67	98.12	94.02	95.71	86.87	91.05	95.43	94.95	93.68	93.75	94.93	93.50	93.90	94.14
Structural formulae based on 22 Oxygen atoms																				
^{IV}Si	6.20	6.22	6.22	6.21	6.14	6.25	6.26	6.23	6.21	6.26	6.32	6.21	6.29	6.29	6.31	6.19	6.24	6.10	6.38	6.18
^{IV}Al	1.80	1.78	1.78	1.79	1.86	1.75	1.74	1.77	1.79	1.74	1.68	1.79	1.71	1.71	1.69	1.81	1.76	1.90	1.62	1.82
Octahedral																				
^{VI}Al	3.81	3.80	3.85	3.64	3.56	3.68	3.58	3.80	3.84	3.86	3.87	3.73	3.74	3.76	3.85	3.82	3.86	3.81	3.71	3.31
Ti	0.09	0.02	0.02	0.04	0.05	0.03	0.03	0.01	0.01	0.01	0.01	0.03	0.03	0.03	0.01	0.01	0.01	0.01	0.01	0.04
Fe	0.05	0.09	0.07	0.25	0.30	0.31	0.25	0.12	0.08	0.08	0.06	0.18	0.17	0.15	0.05	0.11	0.09	0.12	0.07	0.45
Mn	0.00	0.00	0.00	0.00	0.00	0.00	0.00	0.00	0.00	0.00	0.00	0.00	0.00	0.00	0.00	0.00	0.00	0.00	0.00	0.00
Mg	0.09	0.17	0.12	0.21	0.24	0.24	0.29	0.16	0.15	0.11	0.12	0.16	0.16	0.15	0.16	0.17	0.13	0.15	0.28	0.51
SVI	*4.03*	*4.08*	*4.05*	*4.14*	*4.16*	*4.26*	*4.15*	*4.09*	*4.07*	*4.05*	*4.06*	*4.09*	*4.09*	*4.09*	*4.07*	*4.11*	*4.09*	*4.09*	*4.08*	*4.31*
Ca	0.00	0.00	0.00	0.00	0.00	0.00	0.00	0.00	0.00	0.00	0.00	0.00	0.01	0.00	0.00	0.01	0.01	0.01	0.01	0.00
Na	0.59	0.41	0.57	0.22	0.22	0.12	0.23	0.47	0.68	0.67	0.43	0.30	0.32	0.30	0.46	0.38	0.40	0.41	0.26	0.11
K	1.17	1.37	1.21	1.56	1.65	1.37	1.56	1.29	1.10	1.08	1.25	1.52	1.41	1.41	1.22	1.34	1.29	1.46	1.47	1.70
Sr	0.00	0.00	0.00	0.00	0.00	0.00	0.00	0.00	0.00	0.00	0.00	0.00	0.00	0.00	0.00	0.00	0.00	0.00	0.00	0.00
ΣInterlayer	*1.75*	*1.79*	*1.79*	*1.79*	*1.88*	*1.49*	*1.80*	*1.77*	*1.79*	*1.76*	*1.68*	*1.82*	*1.73*	*1.71*	*1.68*	*1.73*	*1.70*	*1.88*	*1.73*	*1.82*
F	0.00	0.00	0.00	0.00	0.00	0.00	0.00	0.00	0.00	0.00	0.00	0.00	0.00	0.00	0.00	0.00	0.00	0.00	0.00	0.00
Cl	0.00	0.00	0.00	0.00	0.01	0.01	0.01	0.00	0.01	0.00	0.03	0.01	0.00	0.01	0.01	0.00	0.01	0.00	0.01	0.01
Si/Al	1.10	1.11	1.10	1.15	1.13	1.15	1.18	1.12	1.10	1.12	1.14	1.13	1.16	1.15	1.14	1.10	1.11	1.07	1.19	1.20

Table 3 (*continued*)

Drill hole	ALD-57	ALD-57	ALD-57	ALD-57	ALD-57	ALD-57	ALD-57	ALD-57	ALD-57	ALD-49	ALD-49	ALD-49	ALD-49	ALD-49	ALD-49	ALD-49	ALD-49	ALD-49	ALD-49	ALD-49	ALD-49
Depth (m)	366	366	366	366	366	366	366	366	366	611	611	611	611	611	611	611	611	611	611	611	611
	2	3	4	5	6	7	8	9	10	1	2	3	4	5	6	7	8	9	10	11	12
Alteration	Phy.	Phy.	Phy.	Phy.	Phy.	Phy.	Phy.	Phy.	Phy.	Phy.	Phy.	Phy.	Phy.	Phy.	Phy.	Phy.	Phy.	Phy.	Phy.	Phy.	Phy.
Lithologie	Andesite	Andesite	Andesite	Andesite	Andesite	Andesite	Andesite	Andesite	Andesite	Porph. 4	Porph. 4	Porph. 4	Porph. 4	Porph. 4	Porph. 4	Porph. 4	Porph. 4	Porph. 4	Porph. 4	Porph. 4	Porph. 4
(wt%)																					
SiO_2	46.66	45.27	46.06	46.94	47.97	46.02	46.54	47.16	46.03	45.75	47.97	45.94	48.93	45.97	46.71	47.15	46.89	46.91	46.84	45.96	47.47
TiO_2	0.34	0.47	0.23	0.50	0.34	0.47	0.39	0.38	0.40	0.27	0.24	0.25	0.18	0.24	0.25	0.27	0.30	0.30	0.33	0.08	0.19
Al_2O_3	33.35	32.54	32.57	30.52	32.30	34.22	32.69	33.51	32.15	32.89	33.99	32.38	33.92	32.15	34.93	32.80	35.01	34.80	35.04	33.22	33.35
^{1}FeO	3.45	3.58	3.40	3.60	1.94	1.93	2.27	1.85	2.45	0.54	0.47	0.93	0.41	0.60	0.77	1.03	1.11	0.84	1.01	0.55	0.54
MnO	0.02	0.00	0.00	0.02	0.00	0.01	0.00	0.02	0.02	0.00	0.00	0.02	0.00	0.01	0.00	0.00	0.00	0.00	0.00	0.00	0.00
MgO	1.77	1.75	2.15	2.72	1.86	1.24	1.63	1.39	1.69	1.35	1.56	1.69	1.48	1.58	1.41	3.56	1.54	1.70	1.53	3.24	2.30
CaO	0.01	0.03	0.00	0.02	0.00	0.00	0.00	0.00	0.32	0.22	0.13	0.14	0.09	0.28	0.02	0.01	0.01	0.00	0.00	0.00	0.00
Na_2O	0.43	0.40	0.42	0.34	0.37	0.46	0.44	0.46	0.38	0.52	0.50	0.41	0.41	0.50	0.60	0.51	0.57	0.63	0.68	0.38	0.36
K_2O	10.22	10.06	10.17	10.25	9.89	10.31	10.21	10.32	9.72	9.48	9.95	9.53	9.81	9.17	10.19	10.24	9.99	10.02	10.36	10.86	10.62
F	n.a	n.a	n.a	n.a	n.a	n.a	n.a	n.a	n.a	n.a	n.a	n.a	n.a	n.a	n.a	n.a	n.a	n.a	n.a	0.84	0.71
Cl	0.00	0.02	0.01	0.01	0.01	0.00	0.01	0.01	0.01	0.05	0.04	0.08	0.05	0.07	0.02	0.01	0.01	0.02	0.01	0.02	0.01
SO_2	0.01	0.04	0.02	0.02	0.01	0.01	0.01	0.02	0.37	0.31	0.20	0.19	0.17	0.36	0.01	0.02	0.03	0.02	0.01	n.a	n.a
P_2O_5	0.00	0.01	0.02	0.01	0.01	0.02	0.01	0.01	0.02	0.03	0.02	0.03	0.06	0.06	0.02	0.01	0.01	0.01	0.01	n.a	n.a
SrO	0.00	0.01	0.01	0.00	0.00	0.03	0.00	0.00	0.00	0.00	0.00	0.02	0.00	0.00	0.00	0.00	0.00	0.00	0.00	n.a	n.a
Total	96.27	94.19	95.05	94.94	94.70	94.74	94.20	95.13	93.55	91.40	95.07	91.60	95.50	90.98	94.92	95.61	95.47	95.26	95.82	95.14	95.55
Structural formulae based on 22 Oxygen atoms																					
^{IV}Si	6.21	6.18	6.22	6.35	6.41	6.18	6.29	6.30	6.29	6.32	6.35	6.34	6.43	6.38	6.21	6.25	6.20	6.22	6.19	6.18	6.31
^{IV}Al	1.79	1.82	1.78	1.65	1.59	1.82	1.71	1.70	1.71	1.68	1.65	1.66	1.57	1.62	1.79	1.75	1.80	1.78	1.81	1.82	1.69
Octahedral																					
^{VI}Al	3.44	3.41	3.40	3.22	3.50	3.60	3.50	3.57	3.47	3.67	3.66	3.60	3.69	3.63	3.69	3.38	3.66	3.65	3.65	3.44	3.54
Ti	0.03	0.05	0.02	0.05	0.03	0.05	0.04	0.04	0.04	0.03	0.02	0.03	0.02	0.03	0.02	0.03	0.03	0.03	0.03	0.01	0.02
Fe	0.38	0.41	0.38	0.41	0.22	0.22	0.26	0.21	0.28	0.06	0.05	0.11	0.04	0.07	0.09	0.11	0.12	0.09	0.11	0.06	0.06
Mn	0.00	0.00	0.00	0.00	0.00	0.00	0.00	0.00	0.00	0.00	0.00	0.00	0.00	0.00	0.00	0.00	0.00	0.00	0.00	0.00	0.00
Mg	0.35	0.36	0.43	0.55	0.37	0.25	0.33	0.28	0.35	0.28	0.31	0.35	0.29	0.33	0.28	0.70	0.30	0.34	0.30	0.65	0.45
SVI	*4.21*	*4.22*	*4.24*	*4.23*	*4.12*	*4.11*	*4.13*	*4.09*	*4.14*	*4.04*	*4.05*	*4.09*	*4.04*	*4.05*	*4.08*	*4.22*	*4.12*	*4.11*	*4.09*	*4.15*	*4.07*
Ca	0.00	0.00	0.00	0.00	0.00	0.00	0.00	0.00	0.05	0.03	0.02	0.02	0.01	0.04	0.00	0.00	0.00	0.00	0.00	0.00	0.00
Na	0.11	0.11	0.11	0.09	0.09	0.12	0.11	0.12	0.10	0.14	0.13	0.11	0.10	0.13	0.15	0.13	0.15	0.16	0.17	0.10	0.09
K	1.74	1.75	1.75	1.77	1.69	1.77	1.76	1.76	1.69	1.67	1.68	1.68	1.64	1.62	1.73	1.73	1.69	1.69	1.75	1.86	1.80
Sr	0.00	0.00	0.00	0.00	0.00	0.00	0.00	0.00	0.00	0.00	0.00	0.00	0.00	0.00	0.00	0.00	0.00	0.00	0.00	0.00	0.00
ΣInterlayer	*1.85*	*1.86*	*1.86*	*1.86*	*1.78*	*1.89*	*1.88*	*1.88*	*1.84*	*1.84*	*1.83*	*1.81*	*1.76*	*1.80*	*1.89*	*1.86*	*1.83*	*1.86*	*1.92*	*1.96*	*1.89*
F	0.00	0.00	0.00	0.00	0.00	0.00	0.00	0.00	0.00	0.00	0.00	0.00	0.00	0.00	0.00	0.00	0.00	0.00	0.00	0.36	0.30
Cl	0.00	0.00	0.00	0.00	0.00	0.00	0.00	0.00	0.00	0.01	0.01	0.02	0.01	0.02	0.00	0.00	0.00	0.00	0.00	0.00	0.00
Si/Al	1.19	1.18	1.20	1.30	1.26	1.14	1.21	1.19	1.21	1.18	1.20	1.20	1.22	1.21	1.13	1.22	1.14	1.14	1.13	1.17	1.21

Table 3 (*continued*)

Drill hole	ALD-43	ALD-43	ALD-43	ALD-43	ALD-43	ALD-43	ALD-43	ALD-43	ALD-43	ALD-43	ALD-43	ALD-43	ALD-43	ALD-43	ALD-43	ALD-43	ALD-43	ALD-43	ALD-43	ALD-43
Depth (m)	907	907	907	907	907	917	917	917	917	917	917	917	917	917	917	917	917	917	917	917
	1	2	3	4	5	1	2	3	4	5	6	7	8	9	10	11	12	13	14	15
Alteration	Phy.	Phy.	Phy.	Phy.	Phy.	Phy.	Phy.	Phy.	Phy.	Phy.	Phy.	Phy.	Phy.	Phy.	Phy.	Phy.	Phy.	Phy.	Phy.	Phy.
Lithologie	Porph. 4	Porph. 4	Porph. 4	Porph. 4	Porph. 4	Porph. 4	Porph. 4	Porph. 4	Porph. 4	Porph. 4	Porph. 4	Porph. 4	Porph. 4	Porph. 4	Porph. 4	Porph. 4	Porph. 4	Porph. 4	Porph. 4	Porph. 4
(wt%)																				
SiO_2	48.10	49.66	47.31	46.89	48.01	49.40	49.40	49.78	50.89	50.92	51.50	50.65	49.84	51.93	47.69	48.19	47.33	47.74	46.31	49.00
TiO_2	0.09	0.12	0.25	0.18	0.11	0.05	0.05	0.04	0.04	0.03	0.05	0.05	0.08	0.06	0.01	0.02	0.11	0.05	0.04	0.05
Al_2O_3	34.50	34.49	34.11	34.04	34.26	32.35	32.34	32.33	33.50	31.79	32.30	32.83	32.56	33.31	35.19	34.32	35.39	34.80	34.21	32.00
^{1}FeO	0.92	0.77	1.24	1.14	1.08	0.10	0.09	0.10	0.12	0.07	0.13	0.23	0.13	0.18	0.96	1.22	2.40	1.18	0.65	1.18
MnO	0.02	0.00	0.00	0.02	0.01	0.03	0.03	0.06	0.03	0.05	0.05	0.05	0.03	0.03	0.00	0.02	0.01	0.03	0.01	0.02
MgO	1.38	1.38	1.17	1.29	1.31	1.91	1.96	2.01	1.76	2.17	2.30	2.00	2.16	2.21	0.87	1.24	0.44	1.09	1.05	1.93
CaO	0.02	0.01	0.01	0.01	0.01	0.13	0.10	0.09	0.15	0.13	0.09	0.21	0.13	0.11	0.01	0.01	0.02	0.01	0.08	0.03
Na_2O	0.48	0.45	0.43	0.47	0.40	0.10	0.10	0.10	0.14	0.12	0.10	0.17	0.14	0.14	0.38	0.37	0.50	0.45	0.43	0.26
K_2O	9.94	9.79	10.00	10.04	10.11	7.98	8.58	8.45	8.09	8.52	8.70	8.45	9.43	8.99	10.15	10.08	10.15	10.19	9.58	10.34
F	n.a	n.a	n.a	n.a	n.a	n.a	n.a	n.a	n.a	n.a	n.a	n.a	n.a	n.a	n.a	n.a	n.a	n.a	n.a	n.a
Cl	0.02	0.01	0.00	0.01	0.01	0.04	0.02	0.04	0.04	0.05	0.03	0.03	0.02	0.01	0.00	0.01	0.00	0.02	0.03	0.01
SO_2	0.07	0.02	0.01	0.01	0.02	0.03	0.04	0.06	0.07	0.09	0.04	0.16	0.15	0.05	0.00	0.02	0.02	0.04	0.21	0.04
P_2O_5	0.06	0.09	0.04	0.05	0.04	0.02	0.02	0.01	0.01	0.02	0.02	0.03	0.03	0.01	0.00	0.00	0.02	0.00	0.02	0.01
SrO	0.00	0.00	0.00	0.02	0.00	0.00	0.00	0.00	0.01	0.00	0.00	0.01	0.01	0.00	0.00	0.00	0.00	0.01	0.00	0.03
Total	95.61	96.77	94.57	94.16	95.38	92.12	92.76	93.09	94.88	93.95	95.30	94.86	94.70	97.04	95.28	95.49	96.40	95.60	92.62	94.91
Structural formulae based on 22 Oxygen atoms																				
^{IV}Si	6.34	6.43	6.31	6.29	6.34	6.61	6.60	6.62	6.61	6.70	6.68	6.62	6.57	6.63	6.30	6.36	6.23	6.30	6.29	6.52
^{IV}Al	1.66	1.57	1.69	1.71	1.66	1.39	1.40	1.38	1.39	1.30	1.32	1.38	1.43	1.37	1.70	1.64	1.77	1.70	1.71	1.48
Octahedral																				
^{VI}Al	3.69	3.70	3.68	3.67	3.68	3.72	3.69	3.68	3.74	3.64	3.63	3.67	3.62	3.64	3.78	3.69	3.73	3.72	3.77	3.53
Ti	0.01	0.01	0.02	0.02	0.01	0.00	0.00	0.00	0.00	0.00	0.00	0.01	0.01	0.01	0.00	0.00	0.01	0.00	0.00	0.01
Fe	0.10	0.08	0.14	0.13	0.12	0.01	0.01	0.01	0.01	0.01	0.01	0.02	0.01	0.02	0.11	0.13	0.26	0.13	0.07	0.13
Mn	0.00	0.00	0.00	0.00	0.00	0.00	0.00	0.01	0.00	0.01	0.01	0.01	0.00	0.00	0.00	0.00	0.00	0.00	0.00	0.00
Mg	0.27	0.27	0.23	0.26	0.26	0.38	0.39	0.40	0.34	0.43	0.44	0.39	0.42	0.42	0.17	0.24	0.09	0.22	0.21	0.38
SVI	*4.08*	*4.06*	*4.07*	*4.08*	*4.07*	*4.12*	*4.10*	*4.10*	*4.11*	*4.08*	*4.10*	*4.10*	*4.07*	*4.09*	*4.06*	*4.08*	*4.09*	*4.07*	*4.06*	*4.05*
Ca	0.00	0.00	0.00	0.00	0.00	0.02	0.01	0.01	0.02	0.02	0.01	0.03	0.02	0.01	0.00	0.00	0.00	0.00	0.01	0.00
Na	0.12	0.11	0.11	0.12	0.10	0.02	0.03	0.03	0.03	0.03	0.03	0.04	0.04	0.04	0.10	0.09	0.13	0.12	0.11	0.07
K	1.67	1.62	1.70	1.72	1.70	1.36	1.46	1.43	1.34	1.43	1.44	1.41	1.59	1.46	1.71	1.70	1.70	1.72	1.66	1.75
Sr	0.00	0.00	0.00	0.00	0.00	0.00	0.00	0.00	0.00	0.00	0.00	0.00	0.00	0.00	0.00	0.00	0.00	0.00	0.00	0.00
ΣInterlayer	*1.79*	*1.73*	*1.81*	*1.84*	*1.81*	*1.41*	*1.50*	*1.47*	*1.40*	*1.48*	*1.48*	*1.48*	*1.64*	*1.52*	*1.81*	*1.79*	*1.84*	*1.83*	*1.79*	*1.83*
F	0.00	0.00	0.00	0.00	0.00	0.00	0.00	0.00	0.00	0.00	0.00	0.00	0.00	0.00	0.00	0.00	0.00	0.00	0.00	0.00
Cl	0.00	0.00	0.00	0.00	0.00	0.01	0.01	0.01	0.01	0.01	0.01	0.01	0.00	0.00	0.00	0.00	0.00	0.00	0.01	0.00
Si/Al	1.18	1.22	1.18	1.17	1.19	1.30	1.30	1.31	1.29	1.36	1.35	1.31	1.30	1.32	1.15	1.19	1.13	1.16	1.15	1.30

Table 3 (*continued*)

Drill hole	ALD-43	ALD-43	ALD-43	ALD-43	ALD-43	ALD-43	ALD-43	ALD-43	ALD-46	ALD-46	ALD-46	ALD-46	ALD-46	ALD-46	ALD-46	ALD-46	ALD-46
Depth (m)	917	917	917	917	869	869	869	869	540	540	540	540	540	540	540	540	540
	16	17	18	19	1	2	3	4	1	2	3	4	5	6	7	8	9
Alteration	Phy.	Phy.	Phy.	Phy.	Phy.	Phy.	Phy.	Phy.	Phy, AA	Phy, AA	Phy, AA	Phy, AA	Phy, AA	Phy, AA	Phy, AA	Phy, AA	Phy, AA
Lithologie	Porph. 4	Porph. 4	Porph. 4	Porph. 4	Porph. 4	Porph. 4	Porph. 4	Porph. 4	Porph. 4	Porph. 4	Porph. 4	Porph. 4	Porph. 4	Porph. 4	Porph. 4	Porph. 4	Porph. 4
(wt%)																	
SiO_2	48.58	49.73	49.74	51.40	50.94	52.30	48.43	48.19	47.05	48.17	44.78	45.72	49.45	47.46	45.85	46.00	45.39
TiO_2	0.02	0.06	0.04	0.05	0.21	0.30	0.22	0.29	0.31	0.30	0.32	0.32	0.13	0.20	0.19	0.20	0.25
Al_2O_3	31.88	33.03	32.49	33.54	36.53	36.89	35.89	34.86	31.70	33.28	32.09	31.86	29.24	35.30	37.00	35.82	36.45
^{1}FeO	2.32	0.19	0.13	0.59	0.48	0.56	0.50	0.59	1.42	0.94	1.32	1.03	0.63	0.47	0.40	0.51	0.47
MnO	0.04	0.02	0.02	0.05	0.02	0.00	0.00	0.01	0.00	0.01	0.00	0.00	0.02	0.01	0.00	0.02	0.03
MgO	2.03	1.84	1.95	1.97	1.14	1.46	0.98	1.10	2.61	1.92	2.23	1.93	3.22	1.02	1.00	0.96	1.03
CaO	0.02	0.03	0.05	0.06	0.02	0.00	0.00	0.01	0.00	0.00	0.01	0.02	0.01	0.09	0.21	0.09	0.19
Na_2O	0.26	0.09	0.12	0.17	0.34	0.26	0.49	0.51	0.33	0.37	0.34	0.54	0.16	0.32	0.36	0.36	0.37
K_2O	9.91	9.75	9.26	9.75	9.40	7.69	10.55	10.62	10.06	10.06	9.75	9.60	9.58	9.31	8.93	9.48	9.47
F	n.a	n.a	n.a	n.a	0.56	0.23	0.23	0.41	n.a	n.a	n.a	n.a	n.a	n.a	n.a	n.a	n.a
Cl	0.01	0.00	0.02	0.01	0.00	0.01	0.00	0.01	0.01	0.01	0.03	0.04	0.03	0.02	0.04	0.04	0.04
SO_2	0.06	0.03	0.08	0.10	n.a	n.a	n.a	n.a	0.01	0.05	0.05	0.52	0.12	0.08	0.14	0.09	0.11
P_2O_5	0.01	0.02	0.01	0.01	n.a	n.a	n.a	n.a	0.01	0.03	0.01	0.01	0.00	0.02	0.02	0.02	0.01
SrO	0.00	0.01	0.00	0.00	n.a	n.a	n.a	n.a	0.00	0.00	0.00	0.00	0.00	0.00	0.04	0.03	0.01
Total	95.11	94.79	93.92	97.71	99.65	99.70	97.29	96.59	93.51	95.15	90.92	91.59	92.61	94.29	94.18	93.62	93.82
Structural formulae based on 22 Oxygen atoms																	
^{IV}Si	6.47	6.54	6.59	6.57	6.39	6.46	6.28	6.31	6.37	6.38	6.24	6.34	6.70	6.29	6.09	6.17	6.08
^{IV}Al	1.53	1.46	1.41	1.43	1.61	1.54	1.72	1.69	1.63	1.62	1.76	1.66	1.30	1.71	1.91	1.83	1.92
Octahedral																	
^{VI}Al	3.48	3.67	3.66	3.63	3.79	3.83	3.76	3.69	3.43	3.58	3.52	3.55	3.37	3.81	3.89	3.83	3.84
Ti	0.00	0.01	0.00	0.00	0.02	0.03	0.02	0.03	0.03	0.03	0.03	0.03	0.01	0.02	0.02	0.02	0.03
Fe	0.26	0.02	0.01	0.06	0.05	0.06	0.05	0.06	0.16	0.10	0.15	0.12	0.07	0.05	0.04	0.06	0.05
Mn	0.00	0.00	0.00	0.01	0.00	0.00	0.00	0.00	0.00	0.00	0.00	0.00	0.00	0.00	0.00	0.00	0.00
Mg	0.40	0.36	0.38	0.37	0.21	0.27	0.19	0.21	0.53	0.38	0.46	0.40	0.65	0.20	0.20	0.19	0.21
SVI	*4.14*	*4.05*	*4.07*	*4.07*	*4.07*	*4.19*	*4.03*	*4.00*	*4.15*	*4.09*	*4.17*	*4.10*	*4.10*	*4.09*	*4.15*	*4.11*	*4.13*
Ca	0.00	0.00	0.01	0.01	0.00	0.00	0.00	0.00	0.00	0.00	0.00	0.00	0.00	0.01	0.03	0.01	0.03
Na	0.07	0.02	0.03	0.04	0.08	0.06	0.12	0.13	0.09	0.10	0.09	0.14	0.04	0.08	0.09	0.09	0.10
K	1.68	1.64	1.56	1.59	1.50	1.21	1.74	1.77	1.74	1.70	1.73	1.70	1.66	1.58	1.51	1.62	1.62
Sr	0.00	0.00	0.00	0.00	0.00	0.00	0.00	0.00	0.00	0.00	0.00	0.00	0.00	0.00	0.00	0.00	0.00
ΣInterlayer	*1.75*	*1.66*	*1.60*	*1.64*	*1.59*	*1.27*	*1.87*	*1.90*	*1.82*	*1.80*	*1.83*	*1.85*	*1.70*	*1.67*	*1.64*	*1.73*	*1.74*
F	0.00	0.00	0.00	0.00	0.22	0.09	0.09	0.17	0.00	0.00	0.00	0.00	0.00	0.00	0.00	0.00	0.00
Cl	0.00	0.00	0.00	0.00	0.00	0.00	0.00	0.00	0.00	0.00	0.01	0.01	0.01	0.01	0.01	0.01	0.01
Si/Al	1.29	1.28	1.30	1.30	1.18	1.20	1.14	1.17	1.26	1.23	1.18	1.22	1.43	1.14	1.05	1.09	1.06

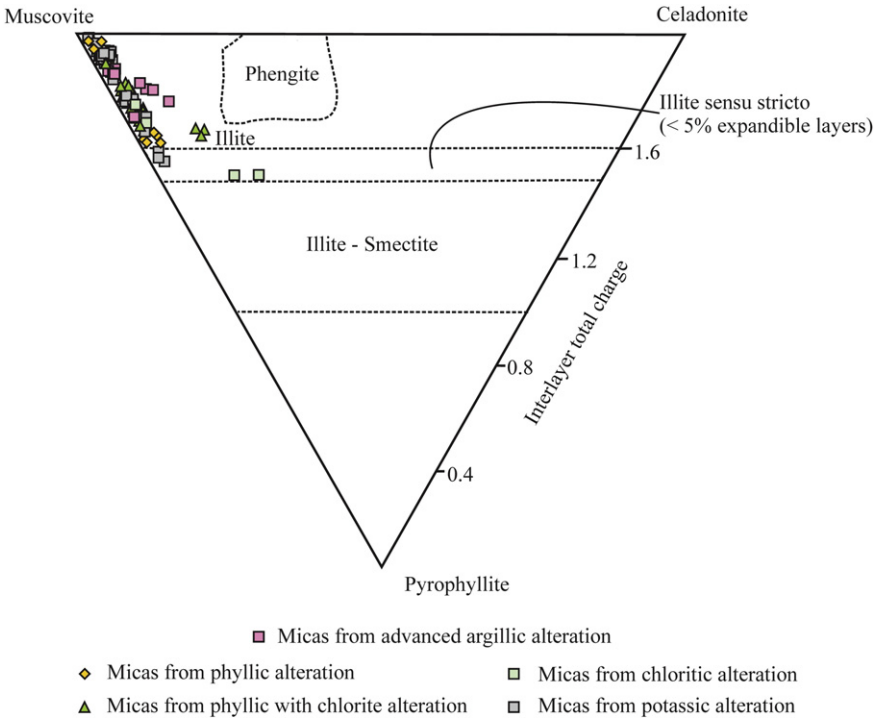

Fig. 10. Classification of dioctahedral phyllosilicates according muscovite-celadonite-pyrophyllite end members (Newman and Brown, 1987).

the wall rocks have intermediate compositions between phlogopite and magnesium biotite (Fig. 5). In general, Si, K, and F (wt.%) show a positive correlation with increased X_{Mg} (Fig. 6B, C, D), whereas Cl shows a negative correlation with increased X_{Mg} (Fig. 6E). Hydrothermal biotite from the wall rocks has less X_{Mg} and K than hydrothermal biotite from porphyries 2 and 4. Hydrothermal biotites from a sample of porphyry

Table 4
Representative Microprobe Analyses of Kaolinite from the Altar deposit.

Sample n°	ALD-46	ALD-46	ALD-46	ALD-46	ALD-46	ALD-46
Depth (m)	540	540	540	540	540	540
	1	2	3	4	5	6
Lithology	Porphyry 4	Porphyry 4	Porphyry 4	Porphyry 4	Porphyry 4	Porphyry 4
Alteration	Advanced argillic	Advanced argillic	Advanced argillic	Advanced argillic	Advanced argillic	Advanced argillic
SiO_2	36.74	38.64	40.09	44.96	44.98	41.89
TiO_2	0.00	0.00	0.00	0.00	0.00	0.00
Al_2O_3	32.44	34.69	35.38	39.06	37.94	35.90
^{1}FeO	0.04	0.07	0.02	0.02	0.02	0.05
MnO	0.00	0.02	0.00	0.00	0.00	0.01
MgO	0.04	0.06	0.04	0.04	0.03	0.03
CaO	0.09	0.13	0.06	0.03	0.02	0.06
Na_2O	0.07	0.08	0.06	0.06	0.06	0.05
K_2O	0.09	0.08	0.14	0.06	0.11	0.13
F	n.a	n.a	n.a	n.a	n.a	n.a
Cl	0.18	0.14	0.14	0.08	0.07	0.12
SO_2	0.34	0.32	0.16	0.10	0.11	0.20
Total	70.12	74.24	76.09	84.41	83.35	78.45
Numbers of cations on basis of O_{10} $(OH)_8$						
Si	3.94	3.92	3.94	3.97	4.00	3.98
^{IV}Al	0.06	0.08	0.06	0.03	0.00	0.02
^{VI}Al	3.88	3.84	3.88	3.93	4.00	3.95
Ti	0.00	0.00	0.00	0.00	0.00	0.00
Fe^{3+}	0.00	0.00	0.00	0.00	0.00	0.00
Mn	0.00	0.00	0.00	0.00	0.00	0.00
Mg	0.01	0.01	0.01	0.01	0.00	0.00
Σ Oct.	3.89	3.85	3.89	3.94	4.00	3.96
K	0.01	0.01	0.02	0.01	0.01	0.01
Ca	0.01	0.01	0.01	0.00	0.00	0.01
Na	0.01	0.02	0.01	0.01	0.01	0.01
F	0.00	0.00	0.00	0.00	0.00	0.00
Cl	0.03	0.02	0.02	0.01	0.01	0.02
Al/Si	1.02	1.02	1.01	1.01	1.00	1.01
R^{3+}/Si	0.99	0.98	0.99	0.99	1.00	1.00

4 at 730 m depth have higher X_{Mg}, Si, and F contents than the hydrothermal biotites from the same porphyry 4 at 142 m depth.

Uchida et al. (2007) suggested that the Al content of biotite can be used to estimate the solidification pressure of the granitic rocks and obtained the empirical equation: P (kb) = 3.03 × TAl − 6.53 (±0.33), where TAl designates the total Al content in biotite on the basis of 22O. Using this geobarometer, the average composition of biotite crystals from Altar indicates a solidification pressure of 1.6 kbar. Biotite from Altar samples falls within the conditions for the X_{Mg}-Ti in biotite geothermometer of Henry et al. (2005) (X_{Mg} = 0.275 − 1.000, Ti = 0.04 − 0.60 atoms per formula unit (apfu), T = 480°−800 °C). However, Altar biotites likely formed at lower pressure (~160 MPa) than the calibration range (400 − 600 MPa). Biotite grains from Altar have X_{Mg} values between 0.60 and 0.87 and Ti between 0.19 and 0.47 atoms per formula. Ilmenite, which is necessary to buffer the TiO_2 chemical potential in the geothermometer (Henry et al., 2005), is an accessory mineral in Altar fresh porphyries. According to this geothermometer, magmatic biotites of porphyry 2 formed at temperatures of ~760–770 °C, magmatic biotites of porphyry 4 at temperatures of 786–801 °C, and magmatic biotites of the barren dacite porphyry formed at 734–754 °C (Fig. 7). The compositions of hydrothermal biotites of porphyries 2 and 4 indicate temperatures of ~771 °C, and between 722 and 799 °C, respectively. Most hydrothermal biotites from the wall rocks reflect temperatures between 690 and 760 °C (Fig. 7).

5.2. Chlorite

Chloritic alteration (chlorite + quartz + dioctahedral potassic phyllosilicates ± rutile) occurs in patches at deep and intermediate levels between the potassic and phyllic alteration types (Fig. 3). Chlorite is also present in the propylitic alteration (chlorite + epidote + calcite ± quartz ± phyllosilicates) that has been mapped in the ridges that surround the district (Fig. 2A). Propylitic alteration is well developed in the andesitic wall rocks, the barren porphyry 1, the barren dacite porphyry, and the late breccia. Table 2 summarizes the chemical composition of hydrothermal chlorites. In this study the structural

Table 5
Clay-size fraction mineralogy and quantification determined by XRD.

Drill hole-Depth (m)	Host rock	Hydrothermal alteration	Clay fraction			Cu (wt.%)	Sample mineralogy (vol %)	Opaque minerals
			Illite (%)	Chl (%)	Kao (%)			
ALD-1-7	Porphyry 4	Phyllic, supergene	90, (IK: 0.31)	10		0.04		hem, jar
ALD-1-58	Porphyry 4	Chloritic, phyllic	20, (IK 0.21)	80		0.45	plag (54), clay (33), gy (3)	py, cpy (hm), dg, cv
ALD-1-86	Porphyry 4	Phyllic, supergene	100, (IK: 0.20)			0.02	qtz (55), clay (37), plag (5), anh (3)	jar
ALD-1-107	Porphyry 4	Phyllic, supergene	100, (IK: 0.38)			0.01	qtz (43), clay (49), plag (5), anh (3)	jar
ALD-1-150	Porphyry 4	Phyllic, supergene	100, (IK: 0.15)			0.01	qtz (72), clay (25), anh (3)	jar
ALD-1-190	Porphyry 4	Chloritic, supergene		100		0.02	plag (64), qtz (17), clay (17), anh (2)	jar
ALD-1-296	Porphyry 4	Phyllic	100, (IK: 0.13)			1.49	qtz (58), clay (37), plag (5)	py, cpy, cv, dg; en
ALD-1-300	Porphyry 4	Phyllic	100, (IK: 0.13)			1.51	qtz (53), clay (41), plag (3), anh (3)	py, cpy, dg, cv
ALD-1-327	Porphyry 4	Phyllic, chloritic	100, (IK: 0.15)			1.04	qtz (63), clay (31), plag (6)	cpy, py, dg, cv
ALD-1-340	Porphyry 4	Chloritic, phyllic	75, (IK: 0.15)	25		1.16	plag (40), qtz (30), clay (30), anh (t)	cpy, py, (hm), dg, cv
ALD-1-353	Porphyry 4	Phyllic	100, (IK: 0.15)	t		0.93	qtz (56), clay (38), plag (3), anh (3)	cpy, py, cv, dg; en
ALD-1-362	Porphyry 4	Phyllic	90, (IK: 0.11)	10		0.78	plag (45), qtz (33), clay (20), anh (2)	cpy, py, dg, cv.
ALD-1-375	Porphyry 4	Phyllic	94, (IK: 0.13)	6		0.41	qtz (64), clay (24), plag (10), anh (2)	cpy, py, dg
ALD-1-382	Porphyry 4	Chloritic, phyllic	90, (IK: 0.15)	10		0.54	clay (39), qtz (33), plag (15), gy (10), anh (2)	cpy, py, dg
ALD-1-406	Porphyry 4	Phyllic	96, (IK: 0.23)	4		0.43	clay (52), qtz (34), gy (10), plag (2), anh (2)	cpy, py, bn, dg, cv
ALD-1-414	Porphyry 4	Phyllic	100, (IK: 0.11)			0.44	clay (66), qtz (27), plag (5), anh (2)	py, cpy, tn; en
ALD-1-444	Porphyry 4	Phyllic	100, (IK: 0.12)			1.84	qtz (55), clay (37), plag (4), anh (4)	py, tn, en
ALD-1-456	Porphyry 4	Phyllic	100, (IK: 0.13)			0.32	qtz (58), clay (34), plag (3), gy (3), anh (2)	py, tn, en
ALD-1-466	Porphyry 4	Phyllic	90, (IK: 0.13)	10		0.46	plag (50), qtz (25), clay (15), gy (8), anh (2)	cpy, py, en
ALD-4-33	Porphyry 2	Phyllic, supergene	100			0.02	qtz (45), plag (19), clay (11), anh (1)	hm, jar, py (t)
ALD-4-67	Porphyry 2	Phyllic, supergene	100			0.01	qtz (50), clay (50)	jar
ALD-4-86	Porphyry 2	Phyllic, supergene	100			0.02	qtz (53), clay(45), plag (2)	jar
ALD-4-135	Porphyry 2	Chloritic		100		0.02	plag (48), qtz (27), clay (25)	jar
ALD-4-148	Porphyry 2	Phyllic, supergene	100			0.01	qtz (35), plag (34), clay (31)	hm
ALD-4-172	Porphyry 2	Phyllic	100			0.28	qtz (55), gy (30), clay (14), plag (1)	cpy, dg, py (t)
ALD-4-299	Porphyry 2	Phyllic	100			0.01	qtz (43), clay (47), ksp (10)	
ALD-4-370	Porphyry 2	Phyllic				0.16	qtz (55), clay (26), plag (15), gy (4)	py
ALD-4-378	Porphyry 2	Chloritic		100		0.24	plag (53), clay (21), qtz (19), gy (7)	cpy, py, hm
ALD-4-387	Porphyry 2	Chloritic				0.24	qtz (47), clay (42), gy (6), plag (3), ksp (2)	py
ALD-4-428	Porphyry 2	Phyllic	90	10		0.41	plag (35), qtz (27), clay (22), anh (13), gy (3)	py, cpy
ALD-4-436	Porphyry 2	Phyllic	90	10		0.64	plag (45), clay (22), qtz (21), anh (10), gy (2)	py, cpy
ALD-4-467	Porphyry 2	Phyllic	100			0.14	qtz (54), clay (30), plag (6), anh (6), gy (3), ksp (1)	py, cpy
ALD-4-477	Porphyry 2	Potassic	90	10		0.19	plag (44), clay (20), qtz (23), anh (12), gy (1)	py, cpy
ALD-4-479	Porphyry 2	Potassic	90	10		0.37	plag (43), qtz (21), anh (20), clay (16)	py, cpy
ALD-4-489	Porphyry 2	Potassic	100			0.30	qtz (49), clay (25), gy (17), plag (6), anh (2)	py, cpy
ALD-4-500	Porphyry 2	Potassic, phyllic	100			0.15	plag (46), qtz (34), clay (10), (5), anh (5)	py, cpy
ALD-43-210	Porphyry 4	Phyllic	100	t		3.32	qtz ≫ clay > plag, ksp, anh, gy (t)	py, cpy, bn, en, dg
ALD-43-229	Porphyry 4	Phyllic	46	40	14	0.76	plag ≫ clay > qtz, gy (t)	py, cpy, tn, en, dg
ALD-43-263	Porphyry 4	Phyllic	77	12	11	0.68	qtz > clay ≫ plag > Ksp, anh, gy (t)	py, cpy, tn, dg, cv
ALD-43-661	Porphyry 4	Potassic	100			1.18	qtz > plag ≫ clay > anh, gy (t)	cpy, py
ALD-43-690	Porphyry 4	Potassic	100	t	t	1.29	plag > qtz ≫ clay = anh, gy (t)	hm, bn, tn, dg, cv
ALD-43-745	Porphyry 4	Potassic	100			1.34	plag > qtz ≫ clay = anh, gy (t)	cpy, py
ALD-43-869	Porphyry 4	Potassic, phyllic	100		t	0.88	plag > qtz ≫ clay = anh, gy (t)	cpy, py, tn (t)
ALD-43-907	Porphyry 4	Phyllic	100	t	t	0.43	plag > qtz ≫ clay = anh, gy (t)	cpy, py, hm

Abbreviations: anh: anhydrite; clay: clay + mica; bn: bornite, kaol: kaolinite, chl: chlorite, cpy: chalcopyrite, cv: covellite; dick: dickite, dg: digenite, en: enargite, gy: gypsum, hm: hematite, ksp: K-feldspar; dpp: dioctahedral potassium phyllosilicate;jar: jarosite, mo: molybdenite, plag: plagioclase, py: pyrite, qtz: quartz, rt: rutile, sl: sphalerite, td: tetrahedrite, tn: tennantite;
tour: tourmaline, t: traces, IK: Kubler index. Numbers in parentheses indicate the proportion determined by methods of quantification.

Table 6
Clay-size fraction mineralogy and quantification determined by XRD

Drill hole-depth (m)	Host rock	Hydrothermal alteration	Clay fraction				Phyllosilicates, mineralogy	Opaque minerals
			Illite (%)	Chl (%)	Kao (%)	Cu (wt%)		
ALD-57-79	Tuff	Supergene	100			0.018	White mica, illite	gold (t)
ALD-57-223	Tuff	Phyllic	100			0.333	White mica, illite	py, en, tn, dg
ALD-57-317	Tuff	Phyllic	100		t	0.211	White mica, illite	hm
ALD-57-338	Andesite	Phyllic	100			0.192	White mica, illite	cpy, py
ALD-57-366	Andesite	Potassic, phyllic	40	40	20	0.299	Biotite, white mica, illite, chlorite, kaolinite	cpy, py
ALD-57-374	Andesite	Potassic, phyllic	100			0.346	Biotite, white mica, illite	cpy, py
ALD-57-622	Andesite	Potassic	100			0.372	Biotite, white mica, illite	cpy, py
ALD-57-672	Porphyry 4	Potassic	100			0.529	Biotite, white mica, illite	cpy, py, tn
ALD-49-77	Porphyry 4	Chloritic, supergene	54	35	11	0.026	White mica, illite, chlorite, kaolinite	py
ALD-49-142	Porphyry 4	Chloritic, supergene	50	38	12	0.786	White mica, illite, chlorite, kaolinite	cpy, py, dg, cv
ALD-49-161	Porphyry 4	Phyllic	100			1.66	White mica, illite	dg
ALD-49-170	Porphyry 4	Phyllic	40	30	30	1.64	White mica, illite, chlorite, kaolinite	dg + cv
ALD-49-192	Porphyry 4	Phyllic	100			0.446	White mica, illite	py
ALD-49-289	Porphyry 4	Phyllic	100			0.799	White mica, illite	py + cpy, tn
ALD-49-483	Porphyry 4	Potassic	100			0.944	Biotite, white mica, illite	cpy, py
ALD-49-498	Porphyry 4	Phyllic	100			0.912	White mica, illite	tn
ALD-49-553	Porphyry 4	Potassic	100			0.658	Biotite, white mica, illite	cpy, py
ALD-49-611	Porphyry 4	Potassic	64	21	15	0.929	Biotite, white mica, illite, chlorite, kaolinite	cpy, py, bn, en, tn
ALD-46-67	Andesite	Phyllic, supergene	100			0.031	White mica, illite	hm
ALD-46-89	Andesite	Phyllic	100			1,283	White mica, illite	cpy, py, dg, cv
ALD-46-107	Andesite	Phyllic	100			2,766	White mica, illite	cpy, tn, dg, cv
ALD-46-246	Andesite	Phyllic	100			0.451	White mica, illite	cpy, py, bn
ALD-46-261	Andesite	Potassic	100	t	t	0.445	Biotite, white mica, illite	cpy, py, bn, hm
ALD-46-271	Andesite	Potassic	100	t	t	0.753	Biotite, white mica, illite	cpy, py
ALD-46-321	Andesite	Chloritic	60	30	10	0.711	White mica, illite, chlorite, kaolinite	cpy, py, en, cv
ALD-46-434	Andesite	Phyllic	100			0.298	White mica, illite	cpy, py
ALD-46-496	Andesite	Phyllic	100			0.438	White mica, illite	cpy, py
ALD-46-540	Andesite	Phyllic	56	38	6	0.485	White mica, illite, chlorite, kaolinite	tn, py, gold (t)
ALD-46-593	Andesite	Potassic	100			0.62	Biotite, white mica, illite	cpy, py, tn, bn
ALD-14-42	Porphyry 4	Phyllic	53	32	15	0.088	White mica, illite	hm
ALD-14-182	Porphyry 4	Phyllic	100			0.094	White mica, illite	cpy, py
ALD-14-317	Late breccia	Phyllic, chloritic	64	20	16	0.369	White mica, illite, chlorite, kaolinite	cpy, tn, dg, cv, hm
ALD-14-353	Late breccia	Phyllic	100			0.202	White mica, illite	cpy, py

Abbreviations: bn: bornite, cpy: chalcopyrite, chl: chlorite, cv: covellite; dg: digenite, kao: kaolinite, en: enargite, hm: hematite, mo: molybdenite, y: pyrite, sl: sphalerite, td: tetrahedrite.

formula of chlorites was recalculated on the basis of $O_{20}(OH)_{16}$ anion content (Newman and Brown, 1987), and all the iron was calculated as Fe^{2+} (Foster, 1962). Microprobe analyses of representative chlorite crystals from the chloritic alteration have the compositional range $(Al_{2.26-3.29}\ Mg_{5.68-7.41}\ Fe^{2+}{}_{1.95-3.44})\ (Si_{5.51-6.03}Al_{1.97-2.49})\ O_{20}\ (OH)_{16}$. Microprobe analyses of representative chlorite crystals from the propylitic alteration have the compositional range $(Al_{2.77-2.46}\ Mg_{5.59-5.39}\ Fe^{2+}{}_{3.31-3.77})\ (Si_{5.51-6.03}Al_{1.71-2.48})\ O_{20}\ (OH)_{16}$. Based on these ranges, the tetrahedral cation composition is between $(Si_{6.29}\ Al_{1.71})$ and $(Si_{5.52}\ Al_{2.48})$, and the octahedral cation totals are between 11.44 and 12.03 per $O_{20}\ (OH)_{16}$ formula unit. Thus, all are trioctahedral chlorites (Foster, 1962; Newman and Brown, 1987).

Plots of chlorite analyses on the diagram of $Fe^{2+}/(Fe^{2+} + Mg)$ versus Si content (Fig. 8A) illustrate the range of chlorite solid solution in both Si-Al and Mg-Fe. All samples plot in the clinochlore field (Bayliss, 1975; Bailey, 1980; McLeod and Stanton, 1984). Within the porphyry 4, chlorite crystals show an increase in Fe and Mn and decrease in Mg contents from the intermediate levels (chloritic alteration) to shallow levels (propylitic alteration, Fig. 8B, Table 2). Chlorite from the altered wall rocks has intermediate Fe content between the two populations of chlorites from porphyry 4. Chlorite from the propylitic alteration of the barren dacite porphyry has high Fe and Si contents (Fig. 8A). Fig. 8B and C present the Fe versus Mg contents and the Al_2O_3 versus X_{Fe} ratios for chlorite and hydrothermal biotite. All chlorites have more Al, and Mg than the biotites, and except for some chlorites from porphyry 4, more Fe than the biotites (Fig. 8B and C).

Chlorite crystallization temperatures (Table 2) were calculated from the equations of Cathelineau (1988), taking into account that the Fe/(Fe + Mg) ratios of the studied chlorites are restricted to a range of 0.22 to 0.39. Chlorite geothermometry is based on empirical observations only, and not equilibrium reactions (Essene and Peacor, 1995). Calculated temperatures of chlorites from chloritic alteration range from 260 to 340 °C (Table 2). Chlorite compositions indicate temperatures between 277 and 337 °C for the propylitic alteration in porphyry 4, and from 214 to 311 °C for the propylitic alteration in the barren dacite porphyry (Table 2). In the MR^3-$2R^3$-$3R^2$ diagram of Fig. 9, all analyzed chlorite crystals plot in the chlorite field defined by Velde (1985).

5.3. Potassic dioctahedral phyllosilicates

Mica-like (>2 μm) + fine grained (<2 μm) dioctahedral potassic phyllosilicates are typically accompanied by quartz ± tourmaline ± rutile in the phyllic alteration that affects all lithologies and forms a continuous halo surrounding the potassic core and the chloritic alteration patches (Figs. 2A and 3). Dioctahedral potassic phyllosilicates are superimposed in potassic alteration, in equilibrium with phyllic and chloritic alterations and cut by advance argillic alteration envelopes.

EPMA data of dioctahedral potassic phyllosilicates were recalculated to atoms per formula unit on the basis of a sum cationic charge of 22 equivalent to O10 $(OH, F, Cl)_2$ anions and all iron was considered as Fe^{2+} (Newman, 1987). The analytical results from 99 microprobe analyses for white micas and clays (summarized in Table 3) are: $K_{1.86-0.95}Na_{0.79-0.02}\ (Al_{3.93-3.22}\ Mg_{0.97-0.04}\ Fe_{0.45-0.00}\ Ti_{0.13-0.0})\ (Si_{7.4-6.08}\ Al_{1.92-0.6})\ O_{10}\ (OH)_4$. Unlike theoretical dioctahedral micas, all analyzed crystals have less K and Na and Si total values in the tetrahedral site exceed 6 (Table 3). The total charge of these micas is less than 2 and this charge difference is compensated by the loss of K. The interlayer cation site occupancy (K + Na + Ca) varies from 1.17 to 1.97 apfu,

most within the range of illite (1.2–1.6 apfu, Table 3) and display an unusually high octahedral occupancy (up to 4.51).

In Fig. 9 (Velde, 1985), most dioctahedral micas present in the potassic and phyllic alterations are close to the composition of muscovite, within the field of illite. Three analyses, one from a sample with potassic alteration and samples with chloritic alteration, plot toward the edge of the montmorillonite. In the muscovite-celadonite-pyrophyllite triangular coordinates (Fig. 10, Velde, 1985; Newman and Brown, 1987), Altar potassic dioctahedral phyllosilicates from all analyzed alteration halos show compositional variations between muscovite and illite.

Of the total analyzed samples (n = 90), illite was identified in 80 samples, making it the most abundant clay mineral in the Altar deposit. In the potassic and chloritic alteration types, the clay fraction is in low proportion and consists of illite and chlorite ± illite, respectively. The clay fraction increases in the phyllic alteration and corresponds to illite (Tables 5 and 6). Based on the illite intensity ratio (Ir), with values between 0.8 and 1.0, no expandable layers were found, except for two samples of illite from the chloritic zone with Ir >1.0 that indicates the presence of <5% smectite. The chemical composition of these illite-bearing assemblages plot in the illite *sensu stricto* field (Fig. 10).

Potassic dioctahedral phyllosilicates in Altar show a range of Al contents that could be explained by a phengitic and illitic substitution vectors (Fig. 11). In the potassic zone with high copper content (>0.8% of Cu, Fig. 11A, B), potassic dioctahedral phyllosilicates show total Al (apfu) between 2.4 and 2.8, whereas those with higher and lower Al contents than this range (2.4–2.8) come from alteration zones with relatively lower Cu grades (0.4–0.6%, Fig. 11A). In the octahedral site, Fe + Mg + Mn contents range from 0.19 to 1.25 apfu; the Mg content varies from 0.04 to 0.97 apfu and the Fe contents between 0 to 0.45 apfu (Table 3). Magnesium content is higher (towards phengitic muscovite composition, >0.5–0.6 apfu) in samples with chloritic alteration and in some samples with potassic alteration (Fig. 11).

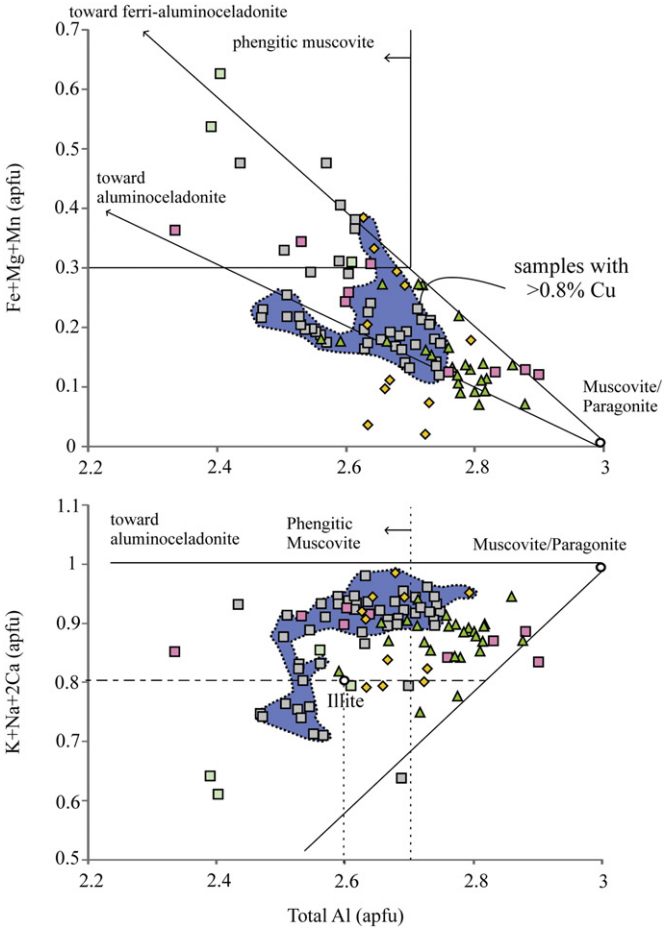

Fig. 11. Compositional variations in white micas: A) Al (apfu) vs. Fe + Mg + Mn (apfu), B) Al (apfu) vs. K + Na + 2Ca (apfu). Arrows represent compositional vectors for main substitution mechanisms and symbols represent end-member compositions.

5.4. Kaolinite

Kaolinite has been identified accompanied by quartz ± rutile in the advanced argillic alteration halos of late veins (E veins). This alteration is poorly developed and generally overlaps zones with phyllic alteration. At depth kaolinite has been recognized cutting potassic alteration zones and forming vein halos (Fig. 3).

The kaolin group (dickite/kaolinite) minerals were differentiated in the X-ray analyses by the reflection of the 001 peak at 7.16 Å and the 002 peak at 3.56 Å, which disappeared when the sample was calcined at 550 °C. The distinction of the kaolinite was based on infrared spectroscopy data by the wavelength absorption feature of 7064, 7115, and 7168 nm. Microprobe analyses of 6 representative kaolinite crystals have the compositional range: $Al_{3.84–4.00}\ Mg_{0.00–0.01}\ (Si_{3.92–4.00}\ Al_{0.00–0.08})\ O_{10}\ (OH_{0.03–10.01})_8$. The structural formula of kaolinite was recalculated on the basis of $O_{10}(OH)_8$ (Newman and Brown, 1987, Table 4). Al: Si and R^{3+}/Si ratios in kaolinite are similar to 1, indicating that kaolinites have relatively small deviations from the ideal formula. Their compositions plot in the field of typical kaolinite in the coordinates MR^3-$2R^3$-$3R^2$ (Fig. 9, Velde, 1985).

6. Discussion

6.1. Implications for the magmas and evolution of the hydrothermal fluids

6.1.1. Magmatic stage and potassic alteration

Distinguishing chemical features of copper-ore-forming calc-alkalic arc magmas include unusually high contents of Sr and V, and unusually low contents of Sc and Y. The Sr/Y and V/Sc ratios are shown to be effective in discriminating least-altered samples of ore-forming intrusions from ordinary, metallogenically unproductive arc magmas (e.g., Loucks, 2014). Altar barren and fertile middle–late Miocene intrusions have a fairly homogeneous andesite-dacite composition and display typical hallmarks of subduction-related magmas such as negative Nb, Ta, P and Ti anomalies (Maydagán et al., 2011). In contrast with the early Miocene lower volcanic complex, high Sr/Y ratios and listric-shaped REE patterns suggest that the andesite and dacite of this suite were derived from magmas that equilibrated with a residual mineralogy dominated by amphibole or amphibole ± garnet (Maydagán et al., 2011). The absence of negative Eu anomalies may be due to high magmatic oxidation states or suppression of plagioclase fractionation due to high pH_2O conditions in the magmas (e.g., Richards et al., 2001; Maydagán et al., 2011).

According the thermobarometer of Ridolfi and Renzulli (2012), amphibole phenocrysts from the barren dacite porphyry are estimated to have crystallized from oxidized magmas (fO_2 = NNO +1 to +2) at temperatures that varied from 780° to 833 °C and pressures between 0.9 and 1.8 kbars (Maydagán et al., 2014) that correspond to depths of ~4 to 7 km in the upper crust. We examined the use of the X_{Mg}-Ti in biotite geothermometer developed by Henry et al. (2005). This geothermometer indicates temperatures of 734–754 °C for the magmatic biotites of the barren dacite porphyry (Fig. 7), which are consistent with its crystallization after amphibole. Based on this geothermometer, magmatic biotites from porphyry 2 and 4 crystallized at slightly higher temperatures (760–770 °C and 786–801 °C, respectively, Fig. 7).

Hydrothermal phlogopite from Altar porphyries replaces magmatic Mg biotite and magmatic amphibole. Brimhall et al. (1985) demonstrated that hydrothermal biotite may be formed from magmatic amphibole

by increased activity or K_2SO_4 or H_2SO_4 (or both) in the hydrothermal fluid.

Fig. 12 shows the X_{Mg} ratio, the K (wt.%), and F (wt.%) contents of magmatic and hydrothermal biotites from Altar porphyries (barren and fertile) in relation to Cu (wt.%) grades of whole rock and meters above sea level. The barren porphyry located 1.5 km from the mineralized center at elevations of ~4000 m.a.s.l. (Fig. 1) has the lowest X_{Mg} and F contents as well as the lowest Cu grade in the whole rock (Fig. 12). The deepest samples analyzed from porphyry 4, in the mineralized core (~2900 masl, Fig. 12), show the highest Cu grades and biotites with the highest X_{Mg} and F contents (Fig. 12). K (wt.%) contents in biotite are more scattered and the highest values were found in magmatic biotite from the deepest samples (~2900 masl), close to the mineralized core (Fig. 12).

In several porphyry Cu deposits, both magmatic and hydrothermal biotite from mineralized porphyries has higher values of the X_{Mg}/X_{Fe} ratio than the biotite from the barren intrusions (Beane, 1974; Brimhall, 1977; Brimhall and Crerar, 1987; Boomeri et al., 2009). Fe/(Fe + Mg) is an indicator of the oxidation state of the host rock and a lower Fe/(Fe + Mg) ratio suggests their crystallization at high oxygen fugacity (Lalonde and Bernard, 1993). Thus, the magmatic biotite crystals from the mineralized porphyries 2 and 4 with lower Fe/(Fe + Mg) ratio probably indicate higher oxygen fugacity in the magma compared to the magmatic biotites from the barren dacite porphyry, which is

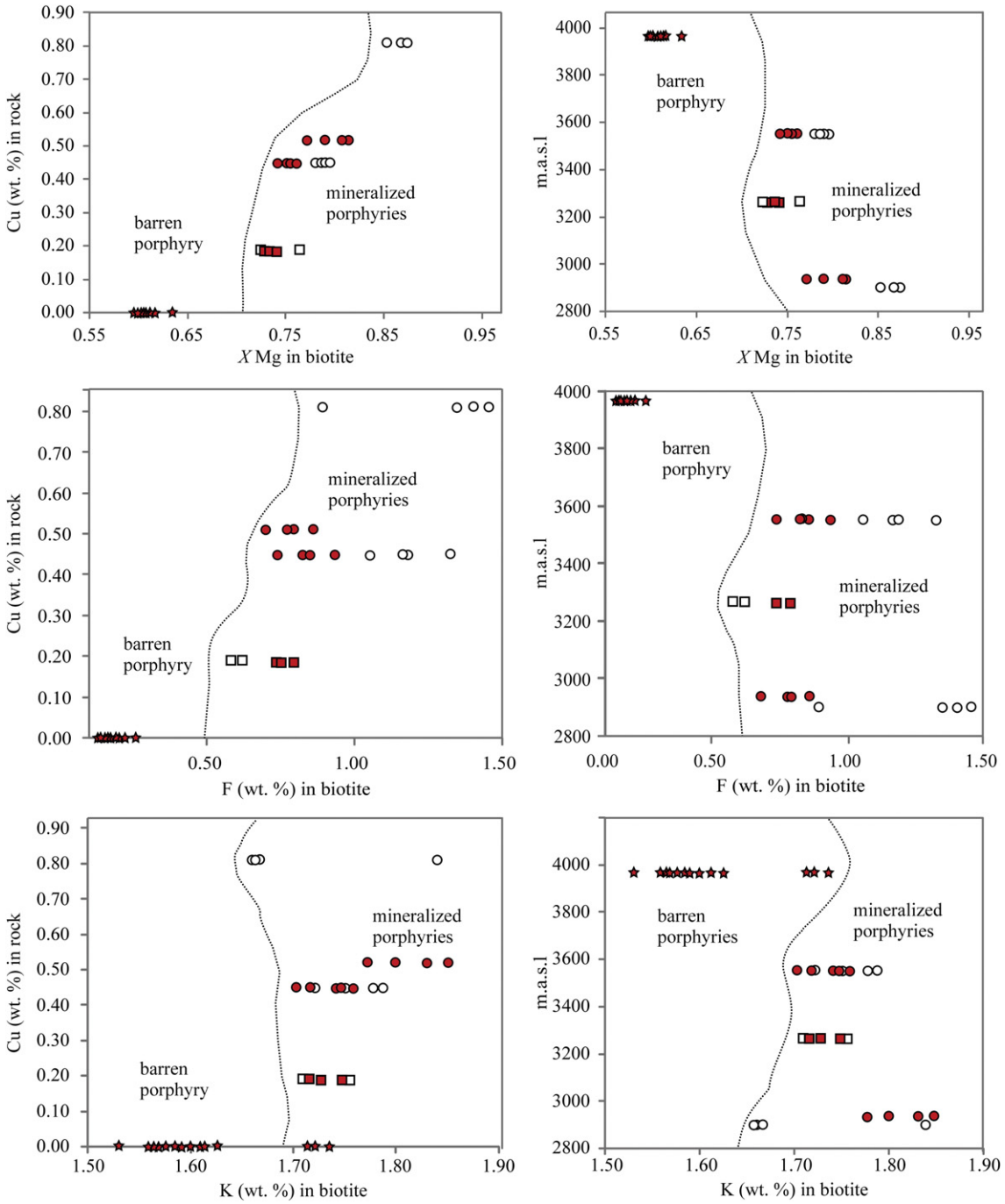

Fig. 12. Compositional variation in biotites. X_{Mg}, F (wt.%) and Ti (wt. %) in biotites are plotted versus Cu (wt.%) content in whole rock and m.a.s.l (meters above sea level).

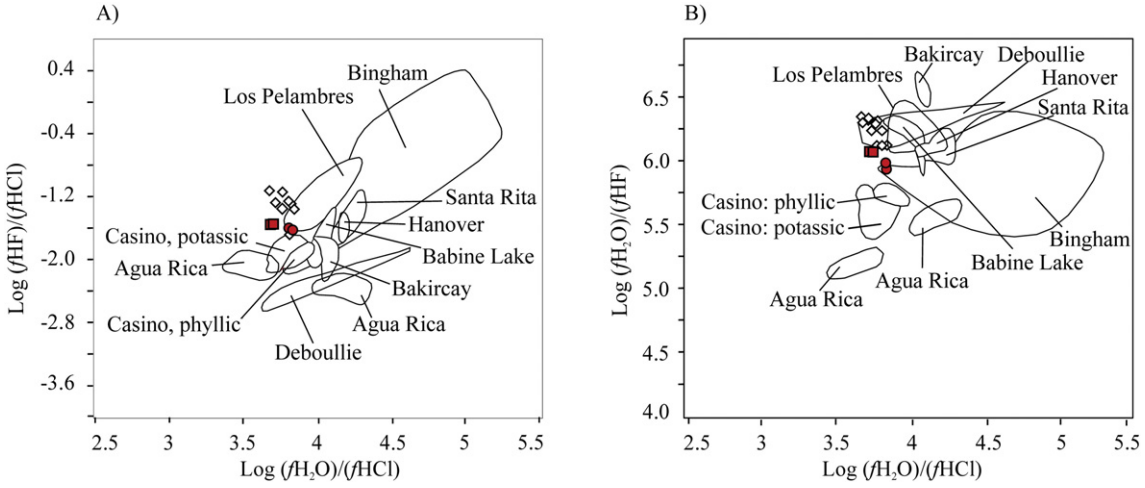

Fig. 13. Log (fHF)/($fHCl$) versus log fH_2O/$fHCl$ and B) Log fH_2O/HF versus log fH_2O/HCl of hydrothermal fluids from the potassic alteration of the Altar deposit, based on the equations of Munoz (1992) and the mean temperature (550 °C) estimated for the potassic alteration from fluid inclusion in early quartz veinlets (Maydagán et al., 2015).

reflected in color differences of the biotites. The Mg-rich character of the magmatic biotite of the porphyries 2 and 4 is consistent with data from other porphyry copper deposits reported in the literature (Jacobs and Parry, 1976, 1979; Beane and Titley, 1981; Selby and Nesbitt, 2000; Boomeri et al., 2009). Magmatic biotites from the mineralized porphyries have higher contents of K and F and lower content of Cl compared to the barren dacite porphyry (Figs. 6C, D, E; 12). These differences may be a function of the geochemical processes associated with the evolution of the melt (Brimhall and Crerar, 1987). The halogen content of biotite has been used to infer the direction of fluid-flow based on the hypothesis that evolving fluids become depleted in F through its preferential partitioning into mineral phases (Gunow et al., 1980; Bath et al., 2013). Higher F concentrations in biotite from the mineralized porphyries provide a tool to track pathways of oxidized, F-bearing fluids (Bath et al., 2013) associated with the mineralization cores in Altar.

Hydrothermal biotite from porphyries 2 and 4 has higher X_{Mg} than hydrothermal biotite from the andesitic wall rocks. This difference may be attributed to changes in fluid composition with time and with distance from the source of the fluid, and to original variations in the mineralogy and geochemistry of the rocks (dacite versus andesite). Enrichment in Mg in the hydrothermal biotite can be attributed to relatively high oxygen and/or sulfur fugacities of the fluid (Wones and Eugster, 1965; Wones, 1972).

The temperatures obtained for hydrothermal biotite assemblages with the X_{Mg}-Ti in biotite thermobarometer (~771 °C in porphyry 2, 722–799 °C in porphyry 4; 690–760 °C in wall rocks) are slightly higher than the temperatures obtained by Ti in quartz geothermometry for the early quartz from type A1 veins (quartz ± potassium feldspar ± chalcopyrite ± pyrite ± rutile veinlets, 670 to 730 °C and depths of 6 to 6.8 km; Maydagán et al., 2015).

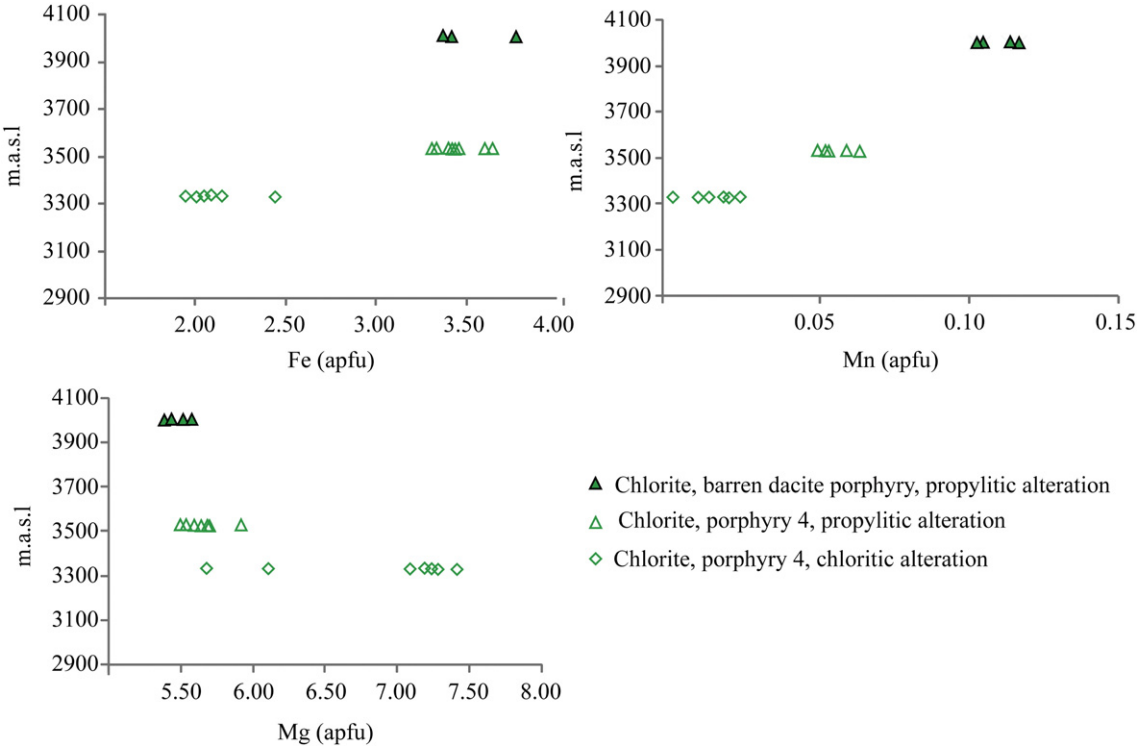

Fig. 14. Compositional variation in chlorites. Fe, Mg, and Mn (wt.%) in chlorites are plotted versus m.a.s.l (meters above sea level).

Fig. 13A and B show the recalculated fugacity ratios of hydrothermal fluids determined from biotite associated with potassic alteration for Altar using the equations of Munoz (1992) and the mean temperature (550 °C) estimated for the potassic alteration from fluid inclusion in early quartz veinlets (Maydagán et al., 2015). This temperature was used in order to compare Altar biotites with recalculated fugacity ratios determined from biotite assemblages associated with potassic alteration from eight porphyry Cu deposits (see Selby and Nesbitt, 2000). Hydrothermal fluids associated with potassic alteration at Altar possessed log fH_2O/HF and log fH_2O/HCl values very similar to those determined for Los Pelambres porphyry Cu deposit of similar age (12.30 and 10.53 Ma, zircon U-Pb ages, Perelló et al., 2012) located 30 km south of Altar. Thus, as suggested previously by Brimhall and Crerar (1987), these ratios may be a function of the magma source and the geochemical processes associated with the evolution of the melt.

6.1.2. Chloritic and phyllic alterations

The principal factor determining chlorite composition is the composition of its ferromagnesian mineral precursor (calcic amphibole or biotite) that generally reflect the characteristics of the host magma (Abdel-Rahman, 1995). The formation of chlorite may have resulted from the destabilization of biotite by the decreasing activity of K_2SO_4 in the hydrothermal fluid at intermediate values of aK^+/aH^+ as the system was cooling (cf. Seedorff et al., 2005). The iron and magnesium content of chlorite is strongly influenced by the concentration of these elements in the parent biotite (e.g., Tulloch, 1979; Czamanske et al., 1981; Parry and Downey, 1982;). Likewise, the Fe/(Fe + Mg) chlorite ratio is also dependant on the bulk composition of the host rock (e.g., Shabani, 2009; Fig. 8)

Wilkinson et al. (2015) indicated that a variety of elements, including K, Li, Mg, Ca, Sr, Ba, Ti, V, Mn, Co, Ni, Zn and Pb, are probably incorporated in the chlorite lattice and display systematic spatial variations relative to the porphyry center. Mg decreases exponentially in concentration with increasing distance, whereas Mn and Fe show evidence for an enrichment halo, or annulus, with peak concentrations at a distance of 1–1.5 km (Wilkinson et al., 2015). Chlorite crystals in Altar show an increase in Fe and Mn and decrease in Mg contents from deep levels associated to copper mineralization (chloritic alteration: Fe 1.95–2.44 apfu, Mg 5.7–7.41 apfu, Mn 0.01–0.03 apfu) to shallow and more distal zones (propylitic alteration: Fe 3.3–3.7 apfu, Mg 5.4–5.6 apfu, Mn 0.10–0.12 apfu, Fig. 14). Similar patterns of proximal Mg enrichment and more distal Fe and Mn enrichment in chlorite, determined by microprobe analysis, were previously reported from the southwest Tintic district (Norman et al., 1991). Factors that could control substitution of elements in chlorite are temperature, chemistry of the protolith rocks, the oxidation state, and the pH of the fluids (e.g., Shikazono and Kawahata, 1987).

We examined the use of the chlorite geothermometer of Cathelineau and Nieva (1985) that is based on the variation in tetrahedral Al content within the chlorite structure according to this equation: $T = -61.92 + 321.98^{*}Al^{IV}$ in chlorites from chloritic and propylitic alteration zones. The temperatures obtained range between 277 ° and 337 °C for the mineralized porphyry (porphyry 4), between 260° and 340 °C for the andesitic wall-rocks and between 214° and 311 °C for the barren dacite porphyry (Table 2). However, De Caritat et al. (1993) indicate that no single chlorite geothermometer performs satisfactorily over the whole range of natural conditions (different temperatures, coexisting assemblages, fO_2) and therefore, chlorite geothermometry should be used only in combination with alternative methods of estimating paleotemperatures.

When projected in the K + Na versus tetrahedral Si diagram, the punctual analyses of potassic dioctahedral phyllosilicates of the phyllic alteration from Altar fall in the same compositional field as those from other porphyry copper deposits worldwide, which display a continuous trend between muscovite and illite composition (Fig. 15, Parry et al., 2002 and references therein Franchini et al., 2012).

Hemley (1959) analyzed the hydrothermal alteration assemblages for the K_2O-Al_2O3-SiO_2-KCl-HCl-H_2O system at 1.0 kbar with quartz present as a function of K^+/H^+ versus temperature (°C). According to this study, Al-rich muscovite is stable in a range of temperatures between 280 and 600 °C and suggest zones of high fluid/rock ratios and acidic fluids. Al poor and Fe rich muscovites suggest near neutral pH conditions, a narrower range of temperature between 280 and 400 °C and a decrease of fluid/rock ratios (higher K^+/H^+ conditions, e.g., Reyes, 1990; Dilles et al., 2000; Mercier-Langevin et al., 2014). Zones with high copper grades (>0.8% Cu) are related to potassic dioctahedral phyllosilicates with intermediate total Al (apfu) contents (between 2.4 and 2.8) and intermediate compositions between muscovite, phengitic muscovite and illite. Ti-in-quartz and fluid inclusion data indicated that pyrite-quartz-muscovite D veins with phyllic haloes formed at temperatures between 425° and 370 °C under hydrostatic pressures of 200 to 350 bars. (Maydagán et al., 2015). Illite may have been formed as the temperature of the hydrothermal fluids decreased below 300 °C (Seedorff et al., 2005), and superposed on mica-like dioctahedral phyllosilicates. We argue that chloritic alteration may have formed at the same time as the phyllic alteration, but further from main fluid flow paths in near neutral conditions. The fluid/rock ratio is lower further from the vein allowing a higher buffering capacity of hydrothermal fluids by the host rocks (Dilles et al., 2000).

6.1.3. Advanced argillic alteration

Late E veins rich in sulfides and sulfosalts that overlapped the deep and intermediate high-temperature veins formed from fluids with lower temperature and pH. These fluids should have caused hydrolysis and the leaching of the alkali phyllosilicate cations forming kaolinite + quartz alteration halos. This alteration suggests that temperature must have dropped locally to ~200 °C to form kaolinite, with a fluid pH <4 (Reyes, 1990).

In the epithermal deposit on the high ridges, vuggy quartz resulted from the leaching of the host rocks by acid fluids with temperatures <250 °C and pH < 2 (Stoffregen, 1987) and the association quartz + alunite + native S indicates temperature of ~360 to 375 °C, very high fO_2 and fS and pH <3 (Stoffregen, 1987; Reyes, 1990; Giggenbach, 1997).

6.2. Metallurgical considerations

The spatial distribution of secondary phyllosilicates (Figs. 2 and 3) is of primary importance for ore processing. One of the most influential factors affecting grinding efficiency and metallurgical results is the presence of clay in the ore (cf. Bulatovic et al., 1999). Aluminosilicate minerals in copper flotation causes different problems, such as (a) loss in recovery, (b) increases of reagent consumption by fine particles; (c) the transfer of large quantities of clay minerals into the concentrate (d) increase in the quantities of fine particles in the crushing and grinding circuits; and (e) the flocculation phenomenon in the froth zone (Bulatovic et al., 1999; Bulatovic, 2007).

Altered frothing properties have been reported as the main reason for the reduced copper flotation recovery (Bulatovic et al., 1999). Montmorillonite has the most deleterious effect on the copper flotation and muscovite also affects the floatability of copper sulfides (Jorjani et al., 2011). To best evaluate and quantify these processes, a greater amount of samples representative of the different alteration and mineralization zones of the Altar deposit have to be analyzed to determine the type and proportion of phyllosilicates, as well as the presence of ore minerals in very fine (<38 μm) and ultra fine (<20 or <10 μm) fractions.

In sectors with low Cu and Mo content in the fine size fraction (<20 μm), it would be possible to use hydro-cyclone for de-sliming and clay removal prior to flotation. In sectors with high Cu and Mo content in the fine size fraction (<20 μm), it would be necessary to

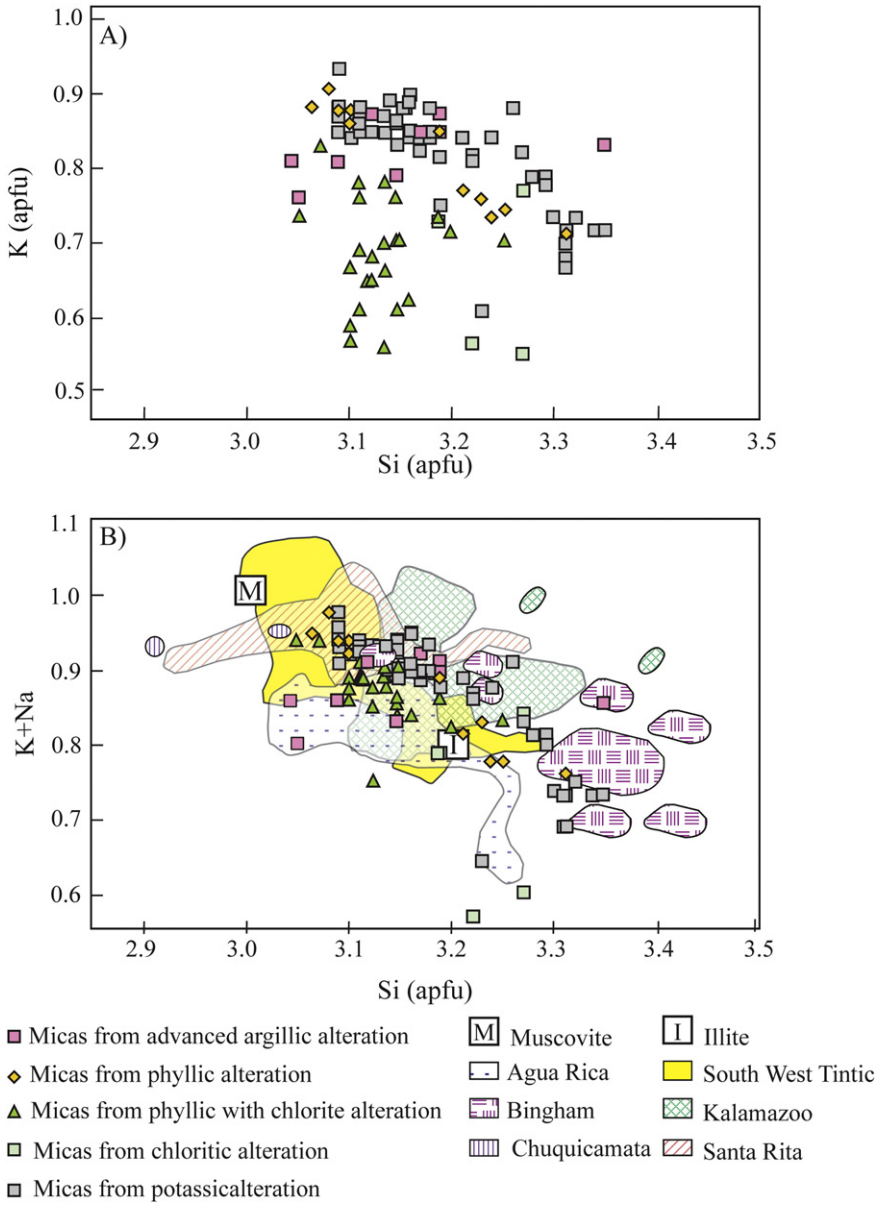

Fig. 15. A) Si versus K for the potassic dioctahedral phyllosilicates of Altar. B) K + versus Na of the potassic dioctahedral phyllosilicates of Altar compared the phyllosilicates from Bingham, Chuquicamata and Kalamazoo (Guilbert and Schafer, 1979), Santa Rita, Bingham and Tintic southwest (Parry et al., 2002), Silbert (Beaufort and Meunier, 1983), and Agua Rica (Franchini et al., 2011).

use a depressing and dispersing agent as $NaSiO_3$ for reduction of clay entrainment during frothing (Farrokhpay and Bradshaw, 2012). As an alternative solution, flotation at reduced pulp density can improve the grade and the recovery of copper and molybdenum and decrease the Al_2O_3 and SiO_2 (Jorjani et al., 2011).

Geometallurgical mapping is a framework to document variability within an orebody and quantify the impact of geology and mineralogy on grinding, metallurgical response and metal recovery processes. The quantitative database obtained can be integrated into 3D block models and is an important tool to reduce technical risk (Williams and Richardson, 2004). Any geometallurgical program should include a systematic mineralogical assessment that has to include a detailed study of mineral association, particle size and liberation characteristics (Williams and Richardson, 2004). Comprehensive liberation and flotation testing should be undertaken in conjunction with mineralogical analysis to optimize and quantify recoveries, separations, grades, and gangue deportment.

7. Conclusions

Phyllosilicates formed throughout hydrothermal evolution responsible for the formation of the Altar Cu–(Au) deposit from early to the latest post mineralization stages. This investigation of the spatial distribution and composition of phyllosilicate minerals and clays outline several distinctive alteration zones, which differ by their hydrothermal history and by their potential behavior during the ore benefaction during metallurgical processing. Using XRD, infrared, and electron microprobe analyses, we detected variations in biotite, chlorite, and potassic dioctahedral phyllosilicate compositions from different zones and depths that can be useful in ore mineral exploration.

X_{Mg}, K, and F contents are higher and the Fe/(Fe + Mg) lower in magmatic biotite of the mineralized porphyries than in the magmatic biotite of the barren porphyries. The lower Fe/(Fe + Mg) ratio in biotite from the mineralized porphyries probably indicates higher oxygen and sulfur fugacities of their magmas.

Hydrothermal biotites from deep levels with potassic alteration and high Cu grades have highest X_{Mg} ratios and high F contents.

Chlorite crystals show an increase in Fe and Mn and decrease in Mg contents from the intermediate levels (chloritic alteration) to shallow and distal zones (propylitic alteration).

Fugacity ratios of hydrothermal fluids determined from Altar biotites are very similar to those determined for biotites in the contemporaneous Los Pelambres deposit (Chile) located 30 km south from Altar. Thus, these parameters may be a function of magma source.

We have used the thermobarometers of Henry et al. (2005) for biotite and of Cathelineau (1988) for chlorite and obtained reasonable temperatures that agree well with previous estimates from Ti in quartz and fluid inclusions.

Potassic dioctahedral phyllosilicate assemblages associated with high copper grades show intermediate compositions between muscovite, phengitic muscovite and illite. The compositional range found in micas reflects a variation in their temperatures of formation, pH, and influence of the fluid/rock ratio from the main channels of fluid flow.

Mineralogical observations and variations in phyllosilicate composition have potential to differentiate between barren and fertile intrusions, to know the temperature of hydrothermal fluids, magma sources, and fluid evolution. Processing of the phyllosilicates, such as illite, kaolinite, and muscovite is problematic, thus systematic optimized testing of proven industrial gangue dispersants, such as sodium silicate and soda ash, should be undertaken. A detailed analysis of type and proportion of phyllosilicates, as well as the presence of ore minerals in these fine fractions, should be done to optimize ore mineral recoveries.

Acknowledgments

This research forms part of a project financed by CONICET (PIP 330), by Universidad Nacional del Comahue (PIN 4-I-209) and an international cooperation program, CONICET-NSF (Res. 1952 del 28/06/2012). We express our appreciation to Roger Rey and the staff of Minera Peregrine Argentina S.A. for site access, logistic support, and help during the field work. David Lentz is supported by Natural Sciences and Engineering Research Council Discovery research grant in Canada.

References

Abdel-Rahman, A.M., 1995. Chlorites in a spectrum of igneous rocks: mineral chemistry and paragenesis. Mineral. Mag. 59, 129–141.

Anderson, M., Alvarado, P., Zandt, G., Beck, S., 2007. Geometry and brittle deformation of the subducting Nazca plate, central Chile and Argentina. Geophys. J. Int. 171, 419–434.

Bailey, S.W., 1980. Summary and recommendations of AIPEA Nomenclature Committee. Clay Clay Miner. 28, 73–78.

Bath, A.B., Walshe, J.L., Cloutier, J., Verrall, M., Cleverley, J.S., Pownceby, M.I., Robinson, P., 2013. Biotite and apatite as tools for tracking pathways of oxidized fluids in the Archean east repulse gold deposit, Australia. Econ. Geol. 108, 667–690.

Bayliss, P., 1975. Nomenclature of the trioctahedral chlorites. Can. Mineral. 13, 178–180.

Beane, 1974. Biotite stability in the porphyry copper environment. Econ. Geol. 69, 241–256.

Beane, R.E., Titley, S.R., 1981. Porphyry copper deposits. Part II. Hydrothermal alteration and mineralization. Econ. Geol. 75th anniversary 235–269 volume.

Beaufort, D., Meunier, A., 1983. A petrographic study of phyllic alteration superimposed on potassic alteration: the Sibert porphyry deposit. Econ. Geol. 78, 1514–1527.

Boomeri, M., Nakashima, K., Lentz, D.R., 2009. The Miduk porphyry Cu deposit, Kerman, Iran: a geochemical analysis of the potassic zone including halogen element systematics related to Cu mineralization processes. J. Geochem. Explor. 103, 17–29.

Brimhall, G.H., 1977. Early fracture controlled disseminated mineralization at Butte, Montana. Econ. Geol. 72, 37–59.

Brimhall, G.H., Crerar, D.A., 1987. Ore Fluids: Magmatic to Supergene. In: Carmichael, I.S.E., Eugster, H.P. (Eds.), Thermodynamic modeling of geological materials: minerals, fluids and melts. Mineralogical Society of America Reviews in Mineralogy 17, pp. 235–321.

Brimhall, G.H., Agee, C., Stoffregen, R., 1985. The hydrothermal conversion of hornblende to biotite. Can. Mineral. 23, 369–379.

Bulatovic, S., 2007. Handbook of Flotation Reagents, Chemistry, Theory and Practice: Flotation of Sulfide Ores. Elsevier Science & Technology Books 0444530290 (446 p).

Bulatovic, S., Wyslouzil, D.M., Kant, C., 1999. Effect of clay slimes on copper, molybdenum flotation from porphyry ores. In: Hancock, B.A., Pen, M.R.L. (Eds.), Proceedings of Copper 99–Cobre 99 International Environment ConferenceMineral Processing/Environment, Health and Safety vol. II. The minerals, Metals and Materials Society.

Cahill, T., Isacks, B., 1992. Seismicity and shape of the subducted Nazca plate. J. Geophys. Res. 97, 17503–17529.

Cathelineau, M., 1988. Cation site occupancy in chlorites and illites as a function of temperature. Clay Miner. 23, 471–485.

Cathelineau, M., Nieva, D., 1985. A chlorite solid solution geothermometer. The Los Azufres (Mexico) geotermal system. Contrib. Mineral. Petrol. 91, 235–244.

Charrier, R., Baeza, O., Elgueta, S., Flynn, J.J., Gans, P., Kay, S.M., Muñoz, N., Wyss, A.R., Zurita, E., 2002. Evidence for Cenozoic extensional basin development and tectonic inversion south of the flat-slab segment, southern Central Andes, Chile (33°–36° S). J. S. Am. Earth Sci. 15, 117–139.

Cohen, J.F., 2011. Mineralogy and geochemistry of hydrothermal alteration at the Ann-Mason porphyry copper deposit, Nevada: Comparison of large-scale ore exploration techniques to mineral chemistry. Unpublished Master thesis, Oregon State University, Oregon, USA, 111p.

Czamanske, G.K., Ishihara, S., Atkin, S.A., 1981. Chemistry of rock-forming minerals of the Cretaceous-Paleocene batholith in southwestern Japan and implications for magma genesis. J. Geophys. Res. 86, 10431–10469.

De Caritat, C.P., Hutcheon, I., Walshe, J.L., 1993. Chlorite geothermometry: a review. Clay Clay Miner. 41, 219–239.

Dilles, J.H., Einaudi, M.T., 1992. Wall-rock alteration and hydrothermal flow paths about the Ann-Mason porphyry copper deposit, Nevada—a 6-km vertical reconstruction. Econ. Geol. 87, 1963–2001.

Dilles, J.D., Proffett, J.M., Einaudi, M.T., 2000. Magmatic and hydrothermal features of the Yerington batholith with emphasis on the porphyry Cu(Mo) deposit in the Ann-Mason area. Soc. Econ. Geol. Guidebook Series 32, 67–89.

Essene, E.J., Peacor, D.R., 1995. Clay minerals thermometry—a critical perspective. Clay Clay Miner. 43, 540–553.

Farías, M., Charrier, R., Carretier, S., Martinod, J., Fock, A., Campbell, D., Cáceres, J., Comte, D., 2008. Late Miocene high and rapid surface uplift and its erosional response in the Andes of central Chile (33°–35°S). Tectonics 27, TC1005. http://dx.doi.org/10.1029/2006TC002046.

Farrokhpay, S., Bradshaw, D.J., 2012. Effect of clay minerals on froth stability in mineral flotation: a review. In 26th International Mineral Processing Congress, IMPC 2012: Innovative Processing for Sustainable Growth-Conference Proceedings, pp. 4601–4611.

Foster, M.D., 1962. Interpretation of the composition and a classification of the chlorites. U.S Geological Survey Professional Paper 414–A, 1–33.

Franchini, M., Impiccini, A., Meinert, L., Grathoff, G., Schalamuk, I.B., 2007. Clay mineralogy and zonation in the Campana Mahuida porphyry Cu deposit, Neuquén, Argentina: implications for porphyry Cu exploration. Econ. Geol. 102, 27–54.

Franchini, M.B., Impiccini, A., Lentz, D., Ríos, F.J., O´Leary, S., Pons, J., Schalamuk, I.A., 2011. Porphyry to epithermal transition in the Agua Rica polymetallic deposit, Catamarca, Argentina: an integrated petrologic analysis of ore and alteration parageneses. Ore Geol. Rev. 41, 49–74.

Franchini, M., Impiccini, A., Beaufort, D., Patrier, P., Anderson, C.G., Pons, J., 2012. Mineral assemblages and distribution of phyllosilicates composition along the main section of the Agua Rica deposit, Catamarca, Argentina: implications for future mine development. Appl. Clay Sci. 67, 61–71.

Gans, C.R., Beck, S.L., Zandt, G., Gilbert, H., Alvarado, P., Anderson, M., Linkimer, L., 2011. Continental and oceanic crustal structure of the Pampean flat slab region, western Argentina, using receiver function analysis: new high-resolution results. Geophys. J. Int. 186, 45–58.

Giggenbach, W.F., 1997. The origin and evolution of fluids in magmatic-hydrothermal systems. In: Barnes, H.L. (Ed.), Geochemistry of Hydrothermal Ore Deposits, 3. Holt Rinehart and Winston, New York, pp. 737–796.

Guilbert, J.M., Schafer, R.W., 1979. Preliminary geochemical characterization of muscovites in porphyry base-metal alteration assemblages. Nevada Bureau of Mines and Geology Report 33 pp. 57–68.

Gunow, A.J., Ludington, S., Munoz, J.L., 1980. Fluorine in micas from the Henderson molybdenite deposit, Colorado. Econ. Geol. 75, 1127–1137.

Gustafson, L.B., Hunt, J.P., 1975. The porphyry copper deposit al El Salvador, Chile. Econ. Geol. 70, 857–912.

Hemley, J.J., 1959. Some mineralogical equilibria in the system K_2O-Al_2O_3-SiO_2-H_2O. Am. J. Sci. 257 (4), 241–270.

Henry, D.J., Guidotti, C.V., Thomson, J.A., 2005. The Ti-saturation surface for low-to-medium pressure metapelitic biotites: implications for geothermometry and Ti-substitution mechanisms. Am. Mineral. 90, 316–328.

Jacobs, D.C., Parry, W.T., 1976. A comparison of the geochemistry of biotite from some basin and range stocks. Econ. Geol. 71, 1029–1035.

Jacobs, D.C., Parry, W.T., 1979. Geochemistry of biotite in the Santa Rita porphyry copper deposit, New Mexico. Econ. Geol. 74, 860–887.

Jordan, T.E., Burns, W., Vega, R., Pángaro, F., Copeland, P., Kelley, S., Mpodozis, C., 2001. Extension and basin formation in the Southern Andes caused by increased convergence rate: a Mid-Cenozoic trigger for the Andes. Tectonics 20, 308–324.

Jorjani, E., Barkhordari, H.R., Khorami, M.T., Fazeli, A., 2011. Effects of aluminosilicate minerals on copper–molybdenum flotation from Sarcheshmeh porphyry ores. Miner. Eng. 24, 754–759.

Kay, S.M., Mpodozis, C., 2002. Magmatism as a probe to the Neogene shallowing of the Nazca plate beneath the modern Chilean flat-slab. J. S. Am. Earth Sci. 15, 39–57.

Kay, S.M., Godoy, E., Kurtz, A., 2005. Episodic arc migration, crustal thickening, subduction erosion, and magmatism in the south-central Andes. Geol. Soc. Am. Bull. 117, 67–88.

Lalonde, A.E., Bernard, P., 1993. Composition and color of biotite from granites: two useful properties in the characterization of plutonic suites from the Hepburn internal zone of Wopmay orogen, Northwest Territories. Can. Mineral. 31, 203–217.

Loucks, R.R., 2014. Distinctive composition of copper-ore-forming arc magmas. Aust. J. Earth Sci. 61 (1), 5–16.
Lowell, J., Guilbert, J., 1970. Lateral and vertical alteration-mineral zoning in porphyry ore deposits. Econ. Geol. 65, 373–408.
Maksaev, V., Munizaga, F., Zentilli, M., Charrier, R., 2009. Fission track thermochronology of Neogene plutons in the Principal Andean Cordillera of central Chile (33–35°S): Implications for tectonic evolution and porphyry Cu-Mo mineralization. Andean Geol. 36, 153–171.
Marek, J.M., 2014. Estimated mineral resources Altar and Quebrada de la Mina deposits. Prepared by Independent Mining Consultants, Inc., for Stillwater Mining Company, Technical Report, San Juan Province Argentina (169 p).
Maydagán, L., 2012. El Prospecto de Cu-(Au-Mo) Altar (31° 29′LS, 70°28′LO), San Juan. Unpublished Ph.D thesis, Universidad Nacional del Sur, Bahía Blanca, Argentina, 340 p.
Maydagán, L., Franchini, M., Chiaradia, M., Pons, J., Impiccini, A., Toohey, J., Rey, R., 2011. Petrology of the Miocene igneous rocks in the Altar Region, Main Cordillera of San Juan, Argentina: a geodynamic model within the context of the Andean flat-slab segment and metallogenesis. J. S. Am. Earth Sci. 32, 30–48.
Maydagán, L., Franchini, M., Chiaradia, M., Dilles, J., Rey, R., 2014. Intrusion history of the Altar porphyry Cu-(Mo-Au) deposit (Argentina): A complex magmatic-hydrothermal system with evidence of recharge processes. Econ. Geol. 109, 621–641.
Maydagán, L., Franchini, M., Rusk, B., Lentz, D., McFarlane, C., Impiccini, A., Ríos, F.J., Rey, R., 2015. Porphyry to epithermal transition in the Altar Cu-(Au-Mo) Deposit, Argentina, studied by cathodoluminescence, LA-ICP-MS, and fluid inclusion analysis. Econ. Geol. 110, 889–923.
McLeod, R.L., Stanton, R.L., 1984. Phyllosilicates and associated minerals in some Paleozoic stratiform sulfide deposits of southeastern Australia. Econ. Geol. 79, 1–22.
Mercer, C., Reed, M., 2013. Porphyry Cu-Mo stockwork formation by dynamic, transient hydrothermal pulses: mineralogic insights from the deposit at Butte, Montana. Econ. Geol. 108, 1347–1377.
Mercier-Langevin, P., Gibson, H.L., Hannington, M.D., Goutier, J., Monecke, T., 2014. A special issue dedicated to Archean magmatism, volcanism, and ore deposits: part 2. Volcanogenic Massive Sulfide Deposits. Econ. Geol. 109, 1–280.
Meyer, C., Hemley, J.J., 1967. Wall Rock Alteration. In: Barnes, H.L. (Ed.), Geochemistry of Hydrothermal Ore Deposits. Holt Rinehart and Winston, New York, pp. 166–235.
Moore, D.M., Reynolds Jr., R., 1997. X-ray diffraction and the identification and analysis of clay minerals. Oxford University Press, New York (378 p).
Mpodozis, C., Cornejo, P., 2012. Cenozoic tectonics and porphyry copper systems of the Chilean Andes. Soc. Econ. Geol. Special Publication 16, 329–360.
Munoz, J.L., 1992. Calculation of HF and HCl fugacities from biotite compositions: revised equations. Geological Society of American, Abstracts with Programs 24 p. 221.
Muñoz, M., Fuentes, F., Vergara, M., Aguirre, L., Nyström, J.O., Féraud, G., Demant, A., 2006. Abanico East Formation: Petrology and geochemistry of volcanic rocks behind the Cenozoic arc front in the Andean Cordillera, central Chile (33°50′S). Rev. Geol. Chile 33, 109–140.
Newman, A., 1987. Chemistry of Clays and Clay Minerals. John Wiley & Sons, Mineralogical Society……, New York.
Newman, A., Brown, G., 1987. In: Newman, A. (Ed.), The chemical constitution of clays. Chemistry of Clays and Clay Minerals, Mineralogical Society Monograph No 6 (129 p).
Norman, D.K., Parry, W.T., Bowman, J.R., 1991. Petrology and geochemistry of propylitic alteration at southwest Tintic, Utah. Econ. Geol. 86, 13–28.
Parry, W.T., Downey, L.M., 1982. Geochemistry of hydrothermal chlorite replacing igneous biotite. Clay Clay Miner. 30, 81–90.
Parry, W.T., Jasumback, M., Wilson, P.N., 2002. Clay mineralogy of phyllic and intermediate argillic alteration at Bingham, Utah. Econ. Geol. 97, 221–239.
Perelló, J., Sillitoe, R.H., Mpodozis, C., Brockway, H., Posso, H., 2012. Geologic setting and evolution of the porphyry copper-molybdenum and copper-gold deposits at Los Pelambres, central Chile. Society of Economic Geologists Special Publication 16 pp. 79–104.
Reider, M., Cavazzini, G., D'yakonov, Y., Frank-Kamenetskii, V., Gottardi, G., Guggenheim, S., Koval, P., Muller, G., Neiva, A., Radoslovich, E., Robert, J., Sassi, F., Takeda, H., Weiss, Z., Wones, D., 1999. Nomenclature of the micas. Mineral. Mag. 63, 267–279.
Reyes, A.G., 1990. Petrology of Philippines geothermal systems and the application of alteration mineralogy to their assessment. J. Volcanol. Geotherm. Res. 43, 279–309.
Richards, J.P., Boyce, A.J., Pringle, M.S., 2001. Geologic evolution of the Escondida area, northern Chile: a model for spatial and temporal localization of porphyry Cu mineralization. Econ. Geol. 96 (2), 271–305.
Ridolfi, F., Renzulli, A., 2012. Calcic amphiboles in calc-alkaline and alkaline magmas: thermobarometric and chemometric empirical equations valid up to 1130 °C and 2.2 GPa. Contrib. Mineral. Petrol. 163, 877–895.
Seedorff, E., Dilles, J.H., Proffett Jr., J.M., Einaudi, M.T., Zurcher, L., Stavast, W.J.A., Johnson, D.A., Barton, M.D., 2005. Porphyry deposits—characteristics and origin of hypogene features: Society of Economic Geologists. Econ. Geol. 100th Anniversary 1905–2005, 251–298.
Selby, D., Nesbitt, B.E., 2000. Chemical composition of biotite from the Casino porphyry Cu–Au–Mo mineralization, Yukon, Canada: evaluation of magmatic and hydrothermal fluid chemistry. Chem. Geol. 171, 77–93.
Shabani, A.A.T., 2009. Mineral chemistry of chlorite replacing biotite from granitic rocks of the Canadian Appalachians. J. Sci., Islamic Republic of Iran 20, 265–275.
Shikazono, N., Kawahata, H., 1987. Compositional differences in chlorite from hydrothermally altered rocks and hydrothermal ore deposits. Can. Mineral. 25, 465–474.
Stoffregen, R.E., 1987. Genesis of acid-sulfate alteration and Au-Cu-Ag mineralization at Summitville, Colorado. Econ. Geol. 82, 1575–1591.
Tulloch, A.J., 1979. Secondary Ca-Al silicates as low-grade alteration products of granitoid biotite. Contrib. Mineral. Petrol. 69, 105–117.
Uchida, E., Endo, S., Makino, M., 2007. Relationship between solidification depth of granitic rocks and formation of hydrothermal ore deposits. Resour. Geol. 57, 47–56.
Velde, B., 1985. Clay minerals: a physico-chemical explanation of their occurrence: Developments in Sedimentology. Elsevier, Amsterdam (427 p).
Wilkinson, J.J., Chang, Z., Cooke, D.R., Baker, M.J., Wilkinson, C.C., Inglis, S., Gemmell, J.B., 2015. The chlorite proximitor: a new tool for detecting porphyry ore deposits. J. Geochem. Explor. 152, 10–26.
Williams, S.R., Richardson, J.M., 2004. Geometallurgical Mapping: a new approach that reduces technical risk. Proceedings of 36th Annual Meeting of the Canadian Mineral Processors. Technical paper 2004-01, pp. 1–13.
Wones, D.R., 1972. Stability of biotite-a reply. Am. Mineral. 57, 316–317.
Wones, D.R., Eugster, H.P., 1965. Stability of biotite-experiment theory and application. Am. Mineral. 50, 1228–1272.
Yáñez, G.A., Ranero, C.R., Huene, R., Díaz, J., 2001. Magnetic anomaly interpretation across the southern central Andes (32–34 S): the role of the Juan Fernández Ridge in the late Tertiary evolution of the margin. J. Geophys. Res. Solid Earth 106, 6325–6345.